Economic Geology, v. 116, no. 7, pp. 1711–1735

CONTROLS ON THE METAL ENDOWMENT OF PORPHYRY Mo DEPOSITS: INSIGHTS FROM THE LUMING PORPHYRY Mo DEPOSIT, NORTHEASTERN CHINA

Hegen Ouyang[1,†] Jingwen Mao,[1,2] Ruizhong Hu,[3,4] John Caulfield,[5] and Zhenhua Zhou[1]

[1]*MNR Key Laboratory of Metallogeny and Mineral Assessment, Institute of Mineral Resources, Chinese Academy of Geological Sciences, Beijing 100037, China*

[2]*China University of Geosciences, Beijing 100083, China*

[3]*State Key Laboratory of Ore Deposit Geochemistry, Institute of Geochemistry, Chinese Academy of Sciences, Guiyang 550081, China*

[4]*College of Earth and Planetary Sciences, University of Chinese Academy of Sciences, Beijing 100049, China*

[5]*Central Analytical Research Facility, Queensland University of Technology, Brisbane 4000, Queensland, Australia*

Abstract

Processes controlling the metal endowment of arc-related porphyry Mo deposits are not well understood. Located in northeastern China, the arc-related Luming porphyry Mo deposit has a proven reserve of 0.75 Mt Mo at an average grade of 0.092 wt % and is characterized by multiple pulses of alteration and mineralization. These features make this deposit an ideal location to investigate the role of multiple pulses of magmatism and fluid release in the evolution and formation of an arc-related porphyry Mo deposit. Molybdenum mineralization at Luming is typically observed as a series of molybdenite-bearing veins hosted within a composite intrusive complex, referred to as the Luming Intrusive Suite. Crosscutting relationships between intrusive units and offset veins indicate that the Luming Intrusive Suite is composed of five major, successive granitic intrusions: the premineralization plutonic biotite monzogranite and monzogranite units, and the synmineralization stock- and dike-like porphyritic monzogranite, granite porphyry, and syenogranite units. Each synmineralization unit is associated with similar vein sequences that comply with the general form of early EB-type biotite veins, through A-type quartz ± biotite and B-type quartz-molybdenite veins, to late D-type quartz-molybdenite ± pyrite ± chalcopyrite, molybdenite, quartz-pyrite ± calcite, and calcite ± clays veins. The intensity and volume of alteration and mineralization within a given synmineralization unit decrease from early- through inter- to late-mineralization units. Although minor Mo mineralization is associated with potassic alteration along B-type veins, the majority of the ore is associated with D-type quartz-molybdenite-pyrite and molybdenite veins rimmed by sericite-chlorite-pyrite alteration, which are primarily hosted in the two premineralization units.

A combination of laser ablation-inductively coupled plasma-mass spectrometry (LA-ICP-MS) zircon U-Pb and hydrothermal biotite $^{40}Ar/^{39}Ar$ studies, together with available isotope dilution-inductively coupled plasma-mass spectrometry (ID-ICP-MS) molybdenite Re-Os data, has resulted in a substantial reappraisal of the timing of magmatism and its association with molybdenite mineralization at Luming. The volumetrically dominant premineralization intrusive units have indistinguishable zircon U-Pb weighted mean $^{206}Pb/^{238}U$ ages ranging from 187.5 ± 2.8 to 186.5 ± 3.6 Ma (2σ), whereas the synmineralization units yield weighted mean $^{206}Pb/^{238}U$ ages from 178.6 ± 2.2 to 175.6 ± 3.0 Ma (2σ). The zircon U-Pb weighted mean $^{206}Pb/^{238}U$ ages of the synmineralization units are indistinguishable from the mean molybdenite Re-Os model (178.1 ± 2.7; 2σ) and hydrothermal biotite $^{40}Ar/^{39}Ar$ plateau (174.7 ± 1.1 Ma; 2σ) ages within uncertainty, confirming a genetic link with mineralization. Melt inclusion data show that the synmineralization intrusions were Mo poor, with Mo concentrations <4 ppm.

The data presented here suggest that molybdenite mineralization at Luming was most likely accomplished through three discrete magmatic-hydrothermal events during assembly of the Mo-poor synmineralization intrusive complex. The giant Luming deposit appears to be related to multiple pulses of magmatic-hydrothermal activities, resulting in the superposition of temporally distinct mineralization events. Our results suggest that pulsed release of ore-forming magmas and fluids, which are channeled along focusing structures like small porphyry fingers within a focused area, from a large magma chamber at depth may play a major role in the formation of large to giant porphyry Mo deposits of both the arc-related and Climax types. This conclusion is in line with field observations of a number of large to giant porphyry Mo deposits, which commonly show reversals in magmatic-hydrothermal evolutionary trend and are associated with multiple pulses of small stocks and dikes that are separate in time and space.

Introduction

Porphyry Mo deposits, together with porphyry Cu-Mo deposits, represent the principal sources of molybdenum on Earth. They are genetically related to deep-seated batholiths, which represent the supply source of the magma, and ore-forming fluids and metals that form the high-level, plug-like ore-forming intrusions and related mineralization (Lowenstern, 1994; Seedorff et al., 2005). It has become evident that porphyry Mo deposits can occur in compressional arc-continent subduction and collision or continent-continent collision and in extensional back-arc, postsubduction, or postcollision settings,

†Corresponding author: e-mail, oyhg1984@163.com

ISSN 0361-0128; doi:10.5382/econgeo.4850; 25 p.
Digital appendices are available in the online Supplements section.

Submitted: August 11, 2020 / Accepted: February 3, 2021

and their size varies significantly (e.g., Carten et al., 1993; Cooke et al., 2005; Ludington and Plumlee, 2009; Mao et al., 2011a; Taylor et al., 2012; Shu et al., 2016; Chen et al., 2017a). Hence, a fundamental question in the study of porphyry Mo deposits is, what processes control the metal endowment of porphyry Mo deposits?

Porphyry Mo deposits were traditionally classified into two major types: (1) Climax-type porphyry Mo deposits associated with fluorine-rich (commonly >1 wt % F), highly evolved rhyolitic intrusions (Carten et al., 1993; Ludington and Plumlee, 2009) and (2) arc-related porphyry Mo deposits associated with fluorine-poor (<0.1 wt % F), differentiated calc-alkaline granitoids (Carten et al., 1993; Taylor et al., 2012). Some major studies have suggested that multiple cycles of mineralization associated with episodic emplacement of causative intrusions is necessary for the formation of large (0.10–0.50 Mt Mo; Chen et al., 2017b) to giant (>0.50 Mt; Chen et al., 2017b) Climax-type porphyry Mo deposits (e.g., Seedorff and Einaudi, 2004; Gaynor et al., 2019a). Compared to Climax-type porphyry Mo deposits, relatively little is known about the processes controlling the metal endowment of arc-related porphyry Mo deposits. This is an important question to answer, because if the metal endowment of porphyry Mo deposits of both the arc-related and Climax type is controlled by common processes, then understanding the mechanisms that lead to the formation of large to giant ore deposits could help with exploration. Otherwise, predicting of the occurrence of large to giant porphyry Mo deposits may be difficult.

The genesis of the largest porphyry deposits (e.g., Cu-Mo-Au, Mo-Cu, and Mo deposits) is proposed to be promoted by various potential factors, including large-volume magma chambers, voluminous ore-forming fluids, long-lived magmatic-hydrothermal activity, high concentrations of ore-forming elements in the magma and ore-forming fluid, efficient partitioning and transport of metals in the magmatic fluid, and localized precipitation of ore-bearing sulfides (e.g., Cooke et al., 2005; Pettke et al., 2010; Richards, 2013; Audétat and Li, 2017; Chelle-Michou et al., 2017; Chiaradia, 2020). A comparison of porphyry Mo-mineralized and barren occurrences reveals that the volumes of the barren Huangshan granite, eastern China, and subeconomic Treasure Mountain granite, western North American, are sufficient to form giant Mo deposits (Lerchbaumer and Audétat, 2013; Zhang and Audétat, 2018). Available melt inclusion data indicate that magmas associated with both porphyry Mo systems and barren felsic intrusions are invariably Mo poor (2–25 ppm; Audétat and Li, 2017; Ouyang et al., 2020). Fluid inclusion data suggest that the compositions of high-temperature single-phase intermediate-density fluids from barren felsic intrusions and mineralized porphyry Mo systems have broadly similar Mo concentrations (~100 ppm; Audétat et al., 2008; Lerchbaumer and Audétat, 2013). The results presented above suggest that the manner in which voluminous ore-forming fluids are drained from depth and delivered to the site of mineralization may exert a dominant control on the metal endowment of porphyry Mo deposits. Nevertheless, the study of the relationship between the metal endowment and the exsolution of fluids from the magmatic system at depth in porphyry Mo systems is usually hindered by the inability to correlate the relative timing of vein formation with the crystallization of the inferred mineralization intrusions. Without this information, the key tectonic, magmatic, and hydrothermal processes responsible for controlling the metal endowment of porphyry Mo systems cannot be fully assessed.

Located in northeastern China, the arc-related Luming porphyry Mo deposit (0.75 Mt Mo at 0.092 wt %; Shao et al., 2012) is part of a Jurassic porphyry-skarn Mo belt in the Zhangguangcai-Lesser Xing'an Range (Fig. 1), which was formed in a continental-arc setting related to the subduction of the Paleo-Pacific plate (Wu et al., 2011). Field observations in the Luming deposit indicate that a genetic relationship exists between the crystallization of discrete magmas and the generation of veins, thus providing an excellent opportunity to investigate the role of cyclic magmatic-hydrothermal events in the precipitation of Mo in porphyry Mo systems. However, previous studies at Luming have not established the temporal relationship between vein formation and intrusion emplacement, which constitutes a crucial constraint necessary to assess the link between venting of fluids from the underlying magma chamber and metal endowment in porphyry Mo systems. In this study, we have reexamined relationships among rock types, hydrothermal alteration, and mineralization by integrating drill core logging, zircon U-Pb and hydrothermal biotite $^{40}Ar/^{39}Ar$ geochronology, and melt inclusion laser ablation-inductively coupled plasma-mass spectrometry (LA-ICP-MS) data at Luming. Our aims are to (1) constrain the sequences of magmatism and mineralization, (2) document the distribution of alteration and mineralization, (3) characterize vein types in terms of mineralogy, alteration, and texture, (4) provide a robust body of geologic evidence to better understand the factors affecting the metal endowment of the arc-related Luming porphyry Mo deposit, and (5) discuss the results of the present study in comparison with the relatively well known Climax-type porphyry Mo deposits.

Geologic Setting

Regional geology

The Luming deposit is found at the northern end of the Zhangguangcai-Lesser Xing'an range (Fig. 1b) and is part of the Central Asian orogenic belt (Fig. 1a), which formed by the amalgamation of a series of microcontinental blocks during the Phanerozoic (Xiao et al., 2003; Wu et al., 2011). Previous studies show that the Zhangguangcai-Lesser Xing'an Range underwent a complex evolutionary history because of its location at the intersection of three tectonic plates (i.e., Paleo-Asian Ocean, Paleo-Pacific Ocean, and Mongolia-Okhotsk Ocean; Wu et al., 2011; Xu et al., 2013). It was formed during two tectonic stages that were primarily controlled by the evolution of the Paleo-Asian Ocean during the Paleozoic to Early Triassic and was overprinted by the subduction of the Paleo-Pacific plate during the Jurassic to Early Cretaceous (Wu et al., 2011). Closure of the Paleo-Asian Ocean at the end of Permian resulted in the EW-oriented regional strike-slip faulting in the southern part of the Zhangguangcai-Lesser Xing'an Range (Fig. 1b; Xiao et al., 2003). The NE-striking strike-slip faults, which crosscut and offset the Mudanjiang-Yilan thrust fault (Fig. 1b), are a consequence of the subduction of the Paleo-Pacific plate (Wu et al., 2011; Xu et al.,

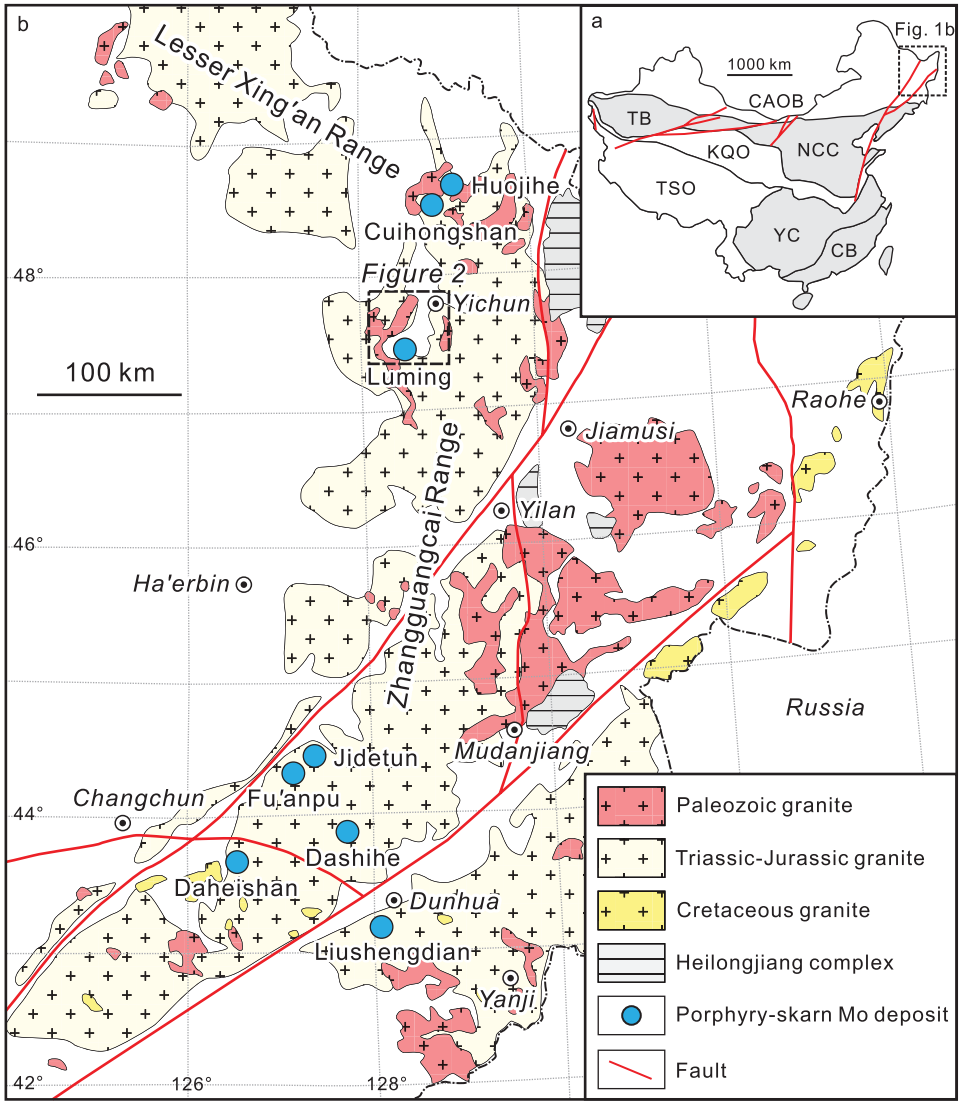

Fig. 1. (a) Simplified geologic map of China showing the location of the Zhangguangcai-Lesser Xing'an Range, northeastern China (modified after Ouyang et al., 2013). (b) Detailed map of the Zhangguangcai-Lesser Xing'an Range (modified after Zhao et al., 2019). Abbreviations: CAOB = Central Asian orogenic belt, CB = Cathaysia block, KQO = Kunlun-Qinling orogen, NCC = North China craton, TB = Tarim block, TSO = Tibet-Sanjiang orogen, YC = Yangtze craton.

2013). Close to the Mudanjiang-Yilan fault, the Heilongjiang Complex (Fig. 1b) is composed of blueschist, serpentinite, greenschist, mica schist, and quartzite and is interpreted as an Early Jurassic accretionary complex that marks the onset of the subduction of the Paleo-Pacific plate beneath northeastern China (Wu et al., 2007).

Phanerozoic granitoids make up the bulk of the Zhangguangcai-Lesser Xing'an Range with rare Paleozoic strata occurring as remnants within the voluminous granitoids (Wu et al., 2011; Xu et al., 2013). Available geochronological data show that granitoids in the Zhangguangcai-Lesser Xing'an Range were emplaced mainly in the early Paleozoic (510–440 Ma), Late Triassic to Middle Jurassic (220–170 Ma), and Early Cretaceous (130–110 Ma; Wu et al., 2011; Xu et al., 2013). The Late Triassic to Middle Jurassic granitoids, which are widespread in the Zhangguangcai-Lesser Xing'an Range (Fig. 1), are composed of arc-related I-type granodiorites and monzogranites. They are associated with economically important porphyry-skarn Mo deposits that show a protracted mineralization history from 187 to 167 Ma (Ouyang et al., 2013), including the Daheishan, Dashihe, Fu'anpu, Liushengdian, Jidetun, Luming, Cuihongshan, and Huojihe porphyry Mo deposits (Fig. 1b). Of these, the Luming deposit is the largest in the range with a proven reserve of 0.75 million metric tons (Mt) Mo at 0.092% (Shao et al., 2012).

District geology

Exposed strata in the Luming district include Cambrian carbonate rocks and Ordovician to Cretaceous volcano-sedimentary sequences (Fig. 2a). Over half of the district is occupied by Jurassic granites with minor Ordovician and rare late Permian to Triassic granites. Dioritic enclaves, which were interpreted as the remnants of mafic magmas, are commonly present throughout the Jurassic granites, indicat-

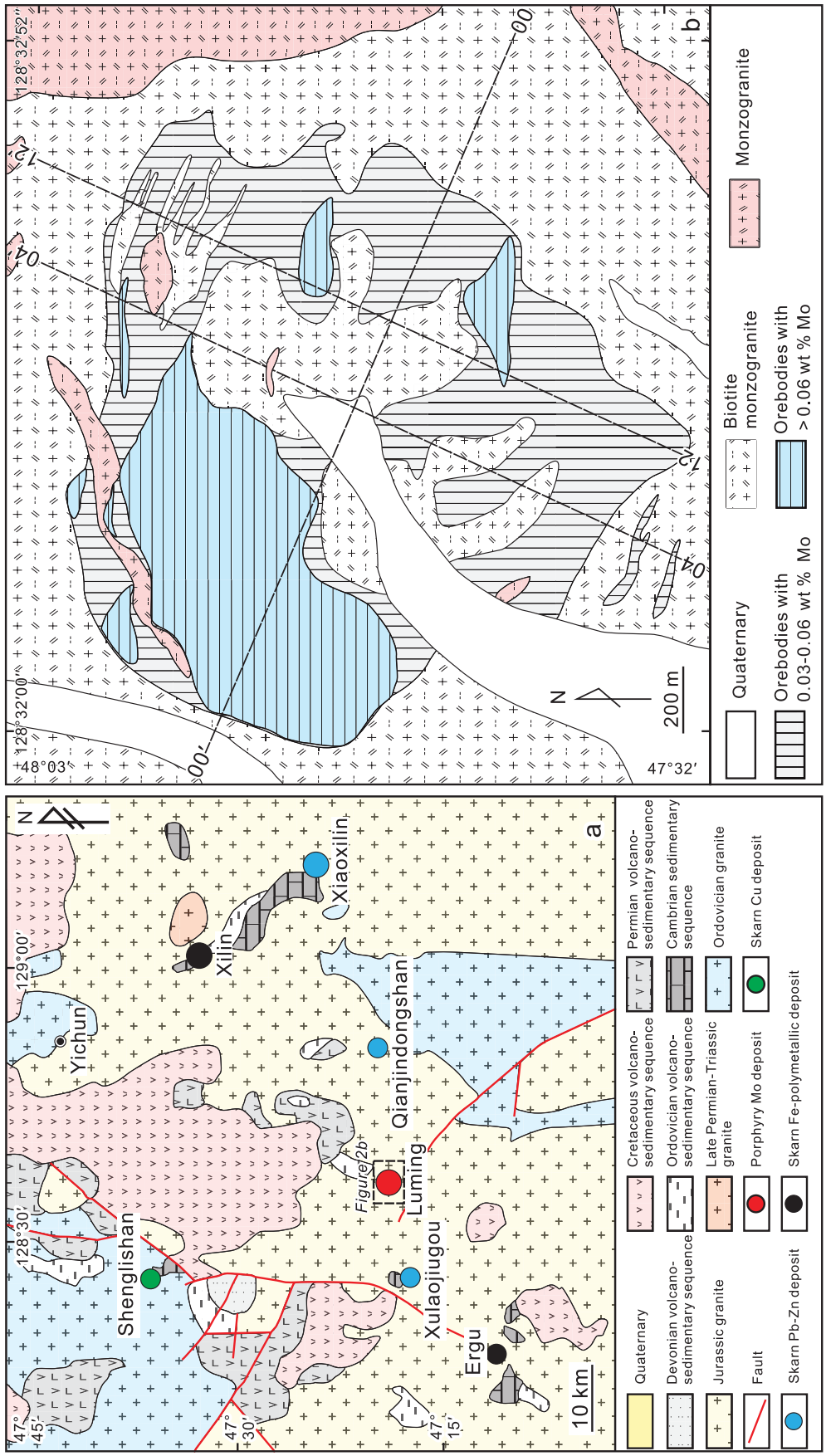

Fig. 2. (a) Simplified district geologic map of the area around the Luming deposit (modified after Shao et al., 2012). (b) Geologic map of the Luming porphyry Mo deposit (modified after Shao et al., 2012). Cross section locations of 0-0′, 4-4′, and 12-12′ are also shown.

ing the involvement of mafic magma in their genesis (Zhu et al., 2017).

Until the discovery of the Luming deposit in 2007, the Luming district was known primarily for Fe, Pb, and Zn, though workers in the 1970s highlighted the district as prospective for porphyry Mo deposits (e.g., F.C. Zhou and B.S. Jin, unpub. report, 1967; X.X. Ye, unpub. report, 1970). Two principal styles of hydrothermal deposits occur in the district: skarn Fe-Pb-Zn-Cu and porphyry Mo (Fig. 2a). Tan et al. (2012) reported a weighted mean molybdenite Re-Os model age of 178.1 ± 1.6 Ma (2σ) for the Luming porphyry Mo deposit. Li et al. (2015) obtained zircon U-Pb weighted mean $^{206}Pb/^{238}U$ ages of 200.0 ± 2.0 and 197.0 ± 2.0 Ma (2σ) for ore-related intrusions from Xilin skarn Fe polymetallic and Xiaoxilin vein Pb-Zn deposits, respectively. More recently, Ouyang et al. (2016) obtained one $^{40}Ar/^{39}Ar$ plateau age of 181.0 ± 4.2 Ma (2σ) for hydrothermal phlogopite from skarn samples in the Ergu deposit. These studies suggest that mineralization in the Luming district spanned a protracted period between 200 and 178 Ma.

Previous Studies

Deposit geology

The geology of the Luming deposit has been described in many previous studies (e.g., Shi et al., 2007; Ma and Chen, 2012; Tan et al., 2012; Hu et al., 2014; Liu et al., 2014; Cheng et al., 2015; Xi et al., 2018). Shi et al. (2007) first documented porphyry-type alteration and Mo mineralization at Luming, which are hosted within a composite pluton, referred to as the Luming Intrusive Suite. Subsequent prospecting and geologic mapping led to the identification of multiple units of the Luming Intrusive Suite (e.g., Shao et al., 2012; Tan et al., 2012). Despite different interpretations on the origin of the host rocks, most early authors agreed that the Luming deposit represents a classic example of a porphyry deposit with mineralization and alteration concentrically zoned around the Luming Intrusive Suite (Fig. 2b). However, prior to this study, no comprehensive geologic accounts of the intrusive activities and hydrothermal features of the deposit have been published, and many aspects of the deposit remain poorly understood. For instance, the units of the Luming Intrusive Suite were proposed to consist of biotite monzogranite, monzogranite, and porphyritic monzogranite (e.g., Hu et al., 2014; Liu et al., 2014; Xi et al., 2018); however, their geometry and spatiotemporal associations between intrusions and veins are not well constrained. Likewise, the distribution of molybdenum within orebodies is poorly documented, such that the causes of zoning in molybdenum grade are not well understood. Additionally, the lower reaches of the system are rarely described, yet multiple lines of evidence indicate that the ore-forming fluids that precipitated molybdenum in the Luming deposit originated from below (e.g., Liu et al., 2014).

Previous geochronology studies on igneous intrusions and Mo mineralization

Attempts to determine the ages of intrusive activity and of Mo mineralization at Luming have been conducted by numerous previous studies (e.g., Ma and Chen, 2012; Tan et al., 2012; Hu et al., 2014; Liu et al., 2014; Cheng et al., 2015; Xi et al., 2018). These age data are summarized in Appendix Tables A1 and A2. Due to the multiple nature of intrusions and attendant mineralization and alteration, together with the possibility of interlaboratory bias inherent in analytical data (e.g., uncertainties in isotopic ratio measurements, fractionation factor calculation using an external standard, and data reduction; e.g., Chiaradia et al., 2013) or different experimental protocols (e.g., Schaltegger et al., 2015), uncertainty remains as to the reconstruction history of the Luming Intrusive Suite and the timing of mineralization. For instance, sensitive high-resolution ion microprobe (SHRIMP) and LA-ICP-MS zircon U-Pb datings of a biotite monzogranite unit yielded two overlapped weighted mean $^{206}Pb/^{238}U$ ages of 201.1 ± 7.8 Ma (2σ, n = 12, mean square weighted deviation [MSWD] = 1.5; Shao et al., 2012) and 194.8 ± 1.4 Ma (2σ, n = 23, MSWD = 2.0; Xi et al., 2018), respectively. Liu et al. (2014) reported a biotite $^{40}Ar/^{39}Ar$ plateau age of 175.9 ± 2.2 Ma (2σ) for the biotite monzogranite unit, which is much younger than corresponding zircon U-Pb weighted mean $^{206}Pb/^{238}U$ ages of 201.1–194.8 Ma (Shao et al., 2012; Xi et al., 2018), possibly resulting from overprinting and resetting by late magmatic-hydrothermal activity. Ma and Chen (2012) and Tan et al. (2012) obtained LA-ICP-MS zircon U-Pb weighted mean $^{206}Pb/^{238}U$ ages for the monzogranite unit of 195.4 ± 2.8 Ma (2σ, n = 13, MSWD = 0.06) and 187.1 ± 2.4 Ma (2σ, n = 14, MSWD = 0.7), respectively, which are older than the weighted mean $^{206}Pb/^{238}U$ ages given by Hu et al. (2014) and Cheng et al. (2015) by up to 15 m.y. using the same method. Ma and Chen (2012), Shao et al. (2012), and Cheng et al. (2015) obtained variable LA-ICP-MS and SHRIMP zircon U-Pb weighted mean $^{206}Pb/^{238}U$ ages of 197.6–182.3 Ma for the porphyritic monzogranite unit, whereas Liu et al. (2014) and Xi et al. (2018) reported appreciably younger LA-ICP-MS zircon U-Pb weighted mean $^{206}Pb/^{238}U$ ages of 174.0 ± 4.0 Ma (2σ, n = 22, MSWD = 3.2) and 176.2 ± 4.2 Ma (2σ, n = 22, MSWD = 0.78), respectively, for the same unit.

Previously reported isotope dilution-inductively coupled plasma-mass spectrometry (ID-ICP-MS) molybdenite Re-Os model ages for molybdenite hosted in the biotite monzogranite and monzogranite units in the form of quartz-molybdenite or molybdenite veins are also highly variable (App. Table A2). Tan et al. (2012), Hu et al. (2014), and Liu et al. (2014) obtained comparable molybdenite Re-Os model ages ranging from 180.0 ± 2.6 to 177.0 ± 2.9 Ma (2σ), whereas Sun et al. (2014) reported older molybdenite Re-Os model ages of 185.9 ± 1.9 to 180.2 ± 5.4 Ma (2σ). More recently, Cheng et al. (2015) reported even younger molybdenite Re-Os model ages of 176.0 ± 2.4 to 178.1 ± 2.51 Ma (2σ).

Methods

Drill core logging and petrography

In this study, field data on intrusive rocks, mineralization, and alteration were collected by logging approximately 8,000 m of previously sampled drill cores from three representative cross sections (00-00′, 04-04′, and 12-12′; Fig. 2b), which penetrate to a depth of up to 600 m below the current ground surface. Vein classification is based on descriptive criteria including morphology, texture, and mineralogy of vein filling and alteration envelopes. The vein terminology (i.e., EB-, A-, B-, and D-type veins) adopted in this study is after Gustafson and Hunt

(1975) and Gustafson and Quiroga (1995). The abundance of veins was recorded in volume percent for each interval of core (~10 cm) based on visual estimates. To document the vein and related hydrothermal alteration assemblages, 197 polished thin sections were visually inspected by petrographic examination under transmitted- and reflected-light microscopy. The temporal evolution of the Luming magmatic-hydrothermal system was determined by observing crosscutting relationships between intrusions and veins and the age of veins relative to each other and to intrusions, together with variations in vein abundance, sulfide mineral ratios, and alteration styles across intrusive contacts. In order to document the spatial changes in ore grade, assay data for three representative cross sections of 00-00′, 04-04′, and 12-12′ sourced from Yichun Luming Ming Co., LTD (unpub. data, 2010) were evaluated.

Zircon U-Pb dating

To better constrain the emplacement history of the Luming Intrusive Suite, representative least altered samples from intrusive units from both drill core and outcrop were selected for LA-ICP-MS zircon U-Pb dating. Zircon grains were handpicked from crushed samples under a binocular microscope after conventional heavy liquid and magnetic separation, and then mounted in epoxy resin. Sample mounts were polished to expose grain centers. The grains were photographed under transmitted and reflected light and then examined using cathodoluminescence (CL) imaging to observe the internal zoned structure of the zircons. Only the rims of the zircon grains were selected for analyses. U-Pb analyses of the zircons were undertaken using a Thermo Fisher X-Series 2 ICP-MS coupled to a Coherent GeoLasPro 193-nm laser at the State Key Laboratory of Geological Processes and Mineral Resources, China University of Geosciences (Beijing). The laser was focused on the sample with a fluency of 5.0 J/cm^2 and a spot of 32-μm diameter at a repetition rate of 6 Hz for 50 s. Helium was used as the carrier gas to transport the ablated aerosol to the mass spectrometer. Zircon Nancy 91500 (Wiedenbeck et al., 1995) was used as the external calibration standard to correct for instrumental mass bias and elemental fractionation. Standard Mud Tank was simultaneously analyzed as an unknown sample, which yielded $^{206}Pb/^{238}U$ ages consistent with the recommended value (727.0 ± 3.8 Ma at 1σ; Black and Gulson, 1978; App. Table A3). The Pb content of zircon was externally calibrated against NIST SRM 610 with Si as an internal standard, whereas other trace elements (e.g., U and Th) were measured with Zr as the internal standard (Hu et al., 2011). Raw data reduction was performed off-line using the ICPMSDataCal software (Liu et al., 2010). The uncertainties of the external standard and decay constant were propagated into the uncertainties of the analyzed samples during the raw data reduction following the methods described by Liu et al. (2010). Concordia diagrams and weighted mean $^{206}Pb/^{238}U$ age calculations were made using Isoplot 3.0 of Ludwig (2003).

Biotite $^{40}Ar/^{39}Ar$ dating

One altered syenogranite sample that contains hydrothermal biotite veinlets from the base of drill core ZK04-04 (Fig. 3a) was selected for $^{40}Ar/^{39}Ar$ dating. About 0.5 g of biotite grains (0.5–2 mm and >99% purity) were handpicked under a binocular microscope and washed with distilled water in an ultrasonic bath and dried. The separates were then wrapped in aluminum foil, stacked in quartz vials along with the ZBH-25 biotite standard (132.7 ± 1.2 Ma at 2σ; Wang, 1983), and irradiated in the 49-2 reactor at the Beijing Atomic Energy Research Institute with a flux of 2.65×10^{13} ncm^{-2}S^{-1} for 24 h, yielding J values of 0.004212 ± 0.0000135 (2σ). The irradiated separates were incrementally heated from 700° to 1,400°C at a rate of 40° to 200°C every 10 min at increasing laser powers in the defocused beam of a 10-W CO_2 laser. The released gas from each step was analyzed on a Helix high-resolution, multicollector (MC) noble gas mass spectrometer at the Institute of Geology, Chinese Academy of Geological Sciences. All measurements were corrected for total system blank, mass spectrometer sensitivity, mass discrimination, and radioactive decay during and subsequent to irradiation, as well as interfering Ar from atmospheric contamination and the irradiation of Ca, Cl, and K. The decay constant for ^{40}K used in the calculation is 5.543×10^{-10} y^{-1} (Steiger and Jäger, 1977). During the calculation of $^{40}Ar/^{39}Ar$ apparent ages on individual step-heating analyses, the uncertainties of J value and decay constant were propagated into the uncertainties of each heating step following the methods described by Chen et al. (2012). The $^{40}Ar/^{39}Ar$ plateau and isochron ages were calculated and plotted using Isoplot 3.0 of Ludwig (2003).

Melt inclusion major and trace element analysis

To document the metal content of discrete units of the Luming Intrusive Suite, melt inclusions hosted in quartz phenocrysts were selected for in situ major and trace analysis by LA-ICP-MS at the Bayerisches Geoinstitut, Germany. Detailed analytical methods have been described by Audétat (2015). Selected melt inclusions from doubly polished thin sections were analyzed with a 193-nm ArF Excimer laser ablation system coupled to a PerkinElmer Elan DRC-e quadrupole ICP-MS. The laser was operated at 5–10 Hz with an energy density of 3–10 J/cm^2 at the sample surface. A beam diameter of 40 μm was used for glasses and quartz hosts, whereas for melt inclusions, the size of the beam was chosen on an individual basis to ensure ablation of the entire melt inclusion but at the same time keeping the amount of ablated host mineral to a minimum. NIST SRM 610 was used as the external standard and was analyzed twice at the beginning and the end of each block of 16 unknowns. A well-characterized in-house obsidian standard was analyzed in each session as an unknown to monitor accuracy. Internal standardization of the melt inclusions was based on SiO_2 versus Al_2O_3 trends defined by the whole-rock data of Ma and Chen (2012), Hu et al. (2014), and Xi et al. (2018).

Results

Geology of the Luming porphyry Mo deposit

In this study, we have reexamined the relationships among rock units of the Luming Intrusive Suite and their related mineralization and alteration, mainly by drill core logging. Through these observations, we have recognized that the geologic relationships at Luming are more complex than previously considered. Details of the Luming deposit geology are summarized in the following sections.

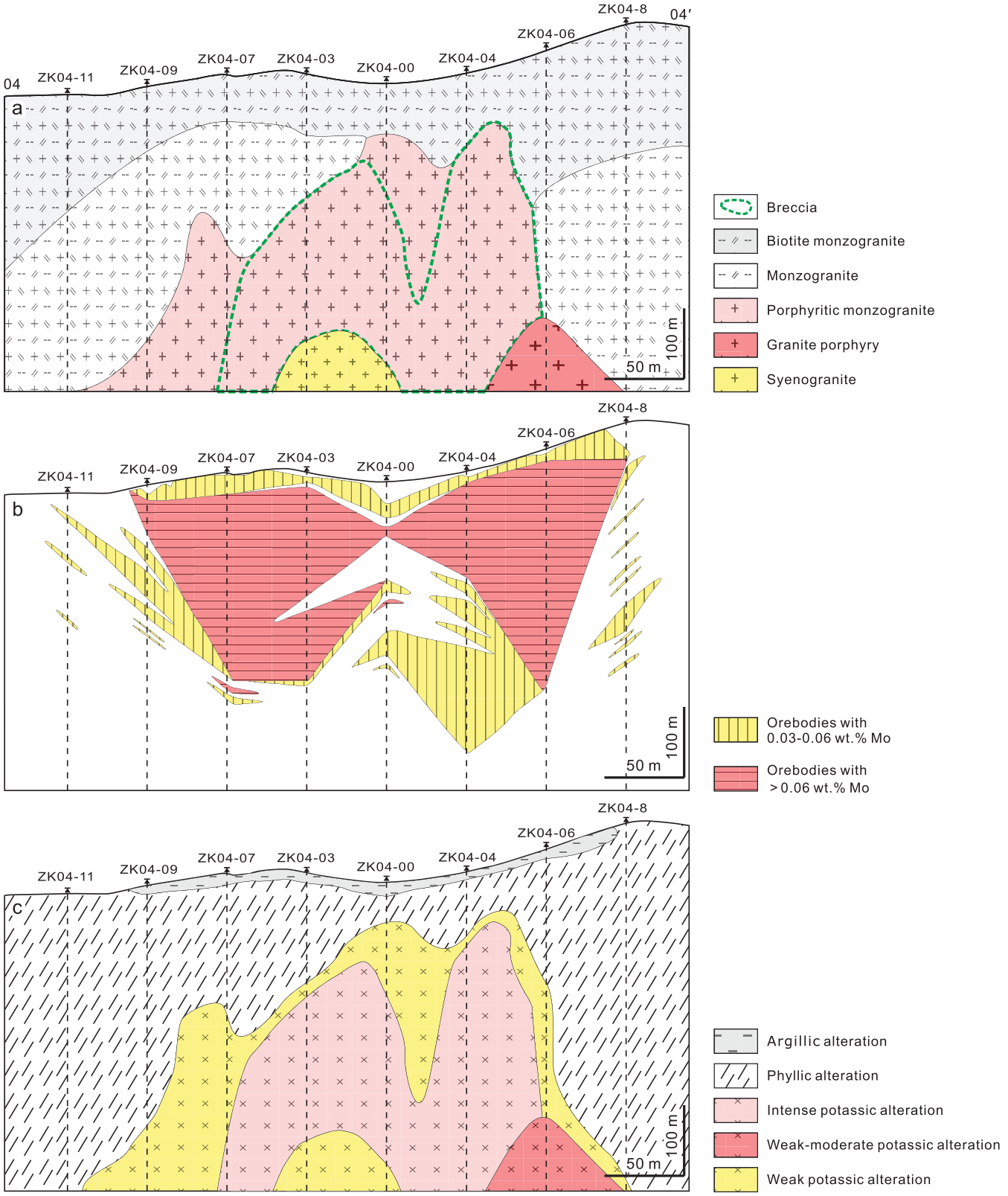

Fig. 3. Geologic cross section 04-04′ of the Luming deposit, showing (a) the crosscutting relationships of the Luming Intrusive Suite, (b) the distribution of Mo grade, and (c) alteration. At least five intrusive units ranging from biotite monzogranite, monzogranite, porphyritic monzogranite, granite porphyry, and syenogranite can be distinguished. Assay data source: Yichun Luming Ming Co., LTD (unpub. data, 2010).

The Luming Intrusive Suite

The Luming Intrusive Suite is a large composite pluton, with a plan area of over 6.5 km² (Fig. 2b). Previous studies have recognized three separate lithological units within the Luming Intrusive Suite: biotite monzogranite, monzogranite, and porphyritic monzogranite (Tan et al., 2012; Hu et al., 2014; Cheng et al., 2015). Our core logging has led to the identification of two previously unrecognized discrete units: granite porphyry and syenogranite. Brief descriptions of individual units are given in Table 1 and their spatial relationships are shown in Figures 3 through 5.

Based on field relationships the oldest intrusion of the Luming Intrusive Suite is the biotite monzogranite unit. It is situated in the uppermost part of the Luming Intrusive Suite (Figs. 3a-5a) and is exposed as a pluton in the mine pit over an area of more than 6.5 km² (Fig. 2b). The unit is light gray, medium grained, and equigranular in texture (Fig. 6a) and is composed of quartz, K-feldspar, plagioclase, and biotite, with minor hornblende (<1 vol %). Hydrothermal alteration and molybdenite-pyrite sulfides are common in the biotite monzogranite unit. Drill core logging data show that the biotite monzogranite unit is the most significant intrusion in the Luming deposit in terms of volume of quartz veining (10–20 vol %; Table 1) and Mo grade (Figs. 3b-5b).

The monzogranite unit (Fig. 6b) is medium grained and contains more K-feldspar but less biotite than the biotite monzogranite (Table 1). It mainly occurs as an unexposed intrusion and forms a flat-topped intrusion into the biotite monzogranite unit (Figs. 2b, 3a-5a). Locally, monzogranite grades into biotite monzogranite, although wherever sharp contacts occur the monzogranite intrudes the biotite monzogranite. In the center part of the mining area, intense quartz veining with elevated Mo grades and sericite and chlorite alteration are common in the monzogranite unit.

The porphyritic monzogranite unit is distinguished by the presence of alkali feldspar megaphenocrysts up to 2 cm in length (Fig. 6c), which contain inclusions of biotite, plagioclase, amphibole, and quartz (Fig. 6d), and of minor volumes of mafic microgranular enclaves (MMEs). It intruded as a central intrusion in the Luming Intrusive Suite and formed a cupola with its apex 100 m below the current surface (Figs. 3a-5a). Along the top of the cupola, fine-grained border phases form irregular bodies as well as dikes intruding into preexisting biotite monzogranite and monzogranite units. They grade downward to normal porphyritic monzogranite. This unit displays quartz veining broadly similar in intensity to that found in the biotite monzogranite unit (Table 1).

The granite porphyry unit (Fig. 6e) was intersected by drill cores extending 450 m below the current ground surface (Figs. 3a-5a). The deep extent of the unit (>600 m) is poorly determined owing to limited drill core data. It is distinguished from other units by its porphyritic texture comprising phenocrysts of K-feldspar, plagioclase, quartz, and biotite (Fig. 6e). This texture suggests emplacement at shallow depth. The unit forms one of the smallest intrusions of the Luming Intrusive Suite and occurs as isolated dikes or plugs intruding the monzogranite and porphyritic monzogranite units. These relationships suggest that the granite porphyry was emplaced later than the monzogranite and porphyritic monzogranite units. Quartz

Table 1. Distinctive Features of Intrusive Units at Luming

Intrusive unit	Texture	Rock-forming mineral (vol %)[1]	Accessory minerals	Crosscutting relationships	Quartz veining (vol %)	Observed vein types	Alteration	Mineralization
Premineralization intrusive complex								
Biotite monzogranite (BMG)	Medium-grained	Qtz: 45–50; Kfs: 15–20; Pl: 20–25; Bt: 5–8; Hbl: <1	Zircon-apatite-titanite-Fe-Ti oxides		10–20%	B- and D-type	Weak K-silicate, intense sericite-chlorite-pyrite, moderate argillic	Intense
Monzogranite (MG)	Medium-grained	Qtz: 45–50; Kfs: 20–25; Pl: 15–20; Bt: <5; Hbl: <1	Zircon-apatite-titanite-Fe-Ti oxides	Crosscut BMG	10–15%	B- and D-type	Weak K-silicate, intense sericite-chlorite-pyrite	Intense
Synmineralization intrusive complex								
Porphyritic monzogranite (PG)	porphyritic	Qtz: 45–50; Kfs: 15–20; Pl: 15–20; Bt: 5–8; Hbl: <2	Zircon-apatite-titanite-Fe-Ti oxides	Crosscut BMG and MG	10–15%	EB-, A-, B-, and D-type	Intense K-silicate, moderate sericite-chlorite-pyrite	Moderate to strong
Granite porphyry (GP)	porphyritic	Qtz: 10–15; Kfs: 15–18; Pl: 10–15; Bt: ~5	Zircon-apatite-titanite-Fe-Ti oxides	Crosscut MG and PC	2–5%	EB-, A-, B-, and D-type	Weak to moderate K-silicate, weak sericite-chlorite-pyrite	Weak to moderate
Syenogranite (SG)	Medium-grained to porphyritic	Qtz: 45–50; Kfs: 25–30; Pl: 15–20; Bt: <3; Hbl: <1	Zircon-apatite-titanite-Fe-Ti oxides	Crosscut PG	<2%	EB- and A-type	Weak K-silicate, weak sericite-chlorite-pyrite	Barren to weak

Abbreviations: Bt = biotite, Hbl = hornblende, Kfs = K-feldspar, Pl = plagioclase, Qtz = quartz
[1]Mineral abundance is estimated from least altered samples of each intrusive phase; biotite estimated refers to magmatic biotite

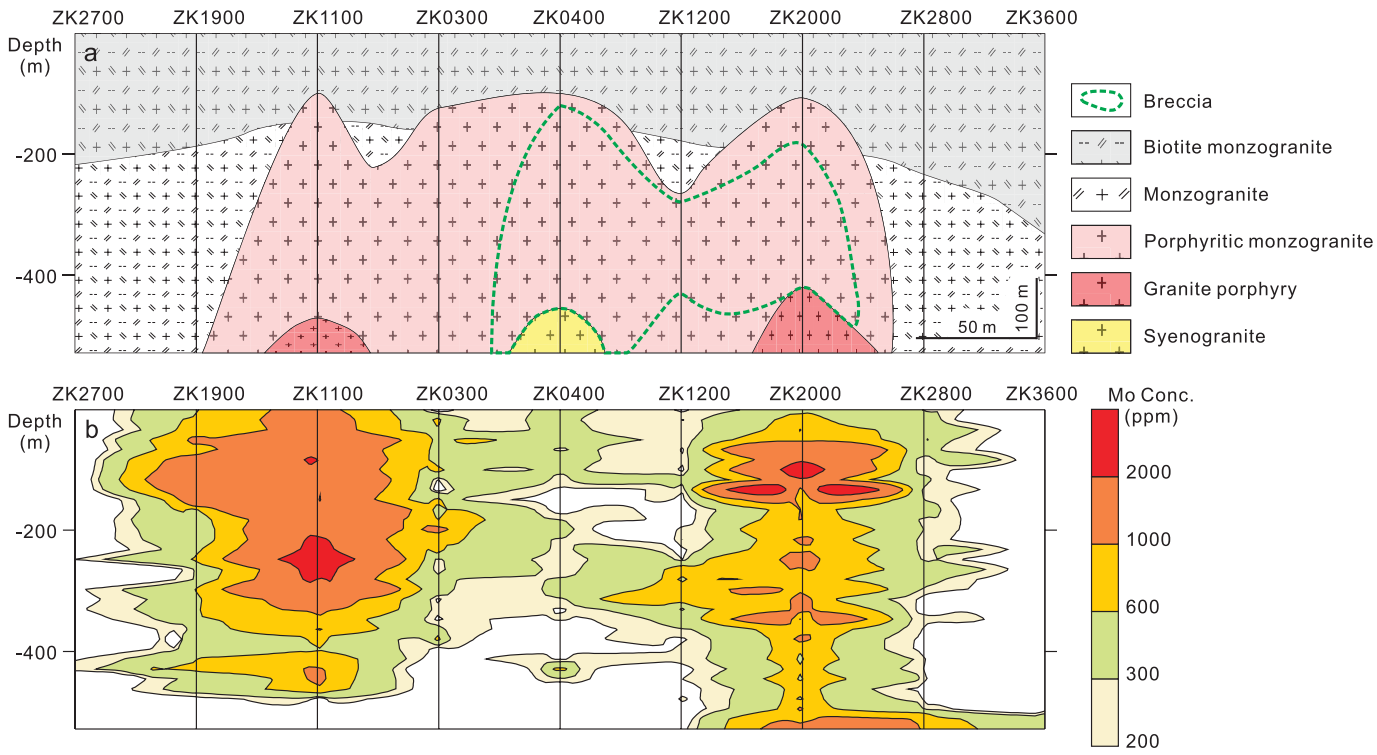

Fig. 4. Geologic cross section 00-00′ of the Luming deposit, showing (a) the crosscutting relationships of the Luming Intrusive Suite and (b) the distribution of Mo grade. Assay data source: Yichun Luming Ming Co., LTD (unpub. data, 2010).

veining and Mo mineralization also affected this unit, albeit with a lower abundance of quartz veining (2–5 vol %; Table 1) and lower Mo grade (Figs. 3b-5b) than the former intrusions.

The syenogranite unit (Fig. 6f) consists of two phases: a border porphyritic phase and an interior medium-grained phase. Everywhere border granite grades downward into the equigranular main interior phase, which indicates the two phases developed contemporaneously. The syenogranite unit has a much stronger red color compared to the other intrusions on account of abundant K-feldspar (Fig. 6f). It is structurally beneath ore-grade mineralization in the mining area and forms the second smallest intrusions of the Luming Intrusive Suite intruding into the porphyritic monzogranite unit (Figs. 3a-5a). The shape of the syenogranite unit at depth is uncertain because the low-grade nature of Mo mineralization associated with this unit did not warrant significant exploration at depth. Although the contact between the syenogranite and granite porphyry units is not revealed by deep drill cores, the lower-degree alteration and low-intensity quartz veins (<2 vol %; Table 1) of the syenogranite unit suggest it is the youngest intrusion of the Luming Intrusive Suite.

Vein stages and distribution

Based on vein truncation relationships and compositions, we have identified a general vein classification sequence consisting of, from early to late, stage 1 EB-type, stage 2 A-type, stage 3 B-type, and stages 4, 5, and 6 D-type veins. Much of the molybdenite occurs in stage 4 D-type veins, but stage 3 B-type veins also contain appreciable amounts of molybdenite. The characteristics, paragenetic sequence, and distribution of each vein type is summarized in Table 2 and Figure 7.

Stage 1 veins (EB-type veins): Stage 1 veins are composed of biotite with K-feldspar envelopes. They are the earliest vein type, occurring with low abundance in the units of porphyritic monzogranite (Fig. 8a, c, g), granite porphyry (Fig. 9a), and syenogranite (Fig. 9e). They are sinuous, ductile in texture, and barren and typically contain thin K-feldspar envelopes (commonly <1 mm in width). Crosscutting relationships show that biotite veins are truncated by later A-, B-, and D-type veins (Figs. 8g, 9a).

Stage 2 veins (A-type veins): Stage 2 veins are most abundant in the porphyritic monzogranite and granite porphyry units and less so in the syenogranite unit, in which two separate types (i.e., A1 and A2) are recognized on the basis of vein composition and crosscutting relationships (Table 2; Fig. 7). A1 veins are less common and are characterized by barren quartz ± biotite veins 1–5 mm in width with no alteration envelopes (Figs. 8a, 9a, c, d). A2 veins are more abundant and consist of quartz with growth zones of K-feldspar (Figs. 8b, d-f, 9a, c, d, f, g). They are typically 1–8 mm in width and cut earlier A1 veins (Fig. 9a). Vein truncation relationships show that both subtypes of stage 2 veins are cut and offset by stage 3 B-type veins, which contain molybdenite and have enclosing K-feldspar envelopes (Figs. 8d, 9a, c). Locally, anomalous vein crosscutting relationships can also be observed; for example, early A2 veins are crosscut by late A2 veins (Fig. 8d), and B-type veins crosscut A1 veins (Fig. 9d).

Stage 3 veins (B-type veins): Stage 3 veins, which make up the final stage in the K-silicate alteration cycle, are distinguished from earlier-stage veins by the occurrence of molybdenite. They represent one of several important molybdenite-bearing vein types at Luming. B-type veins are most common

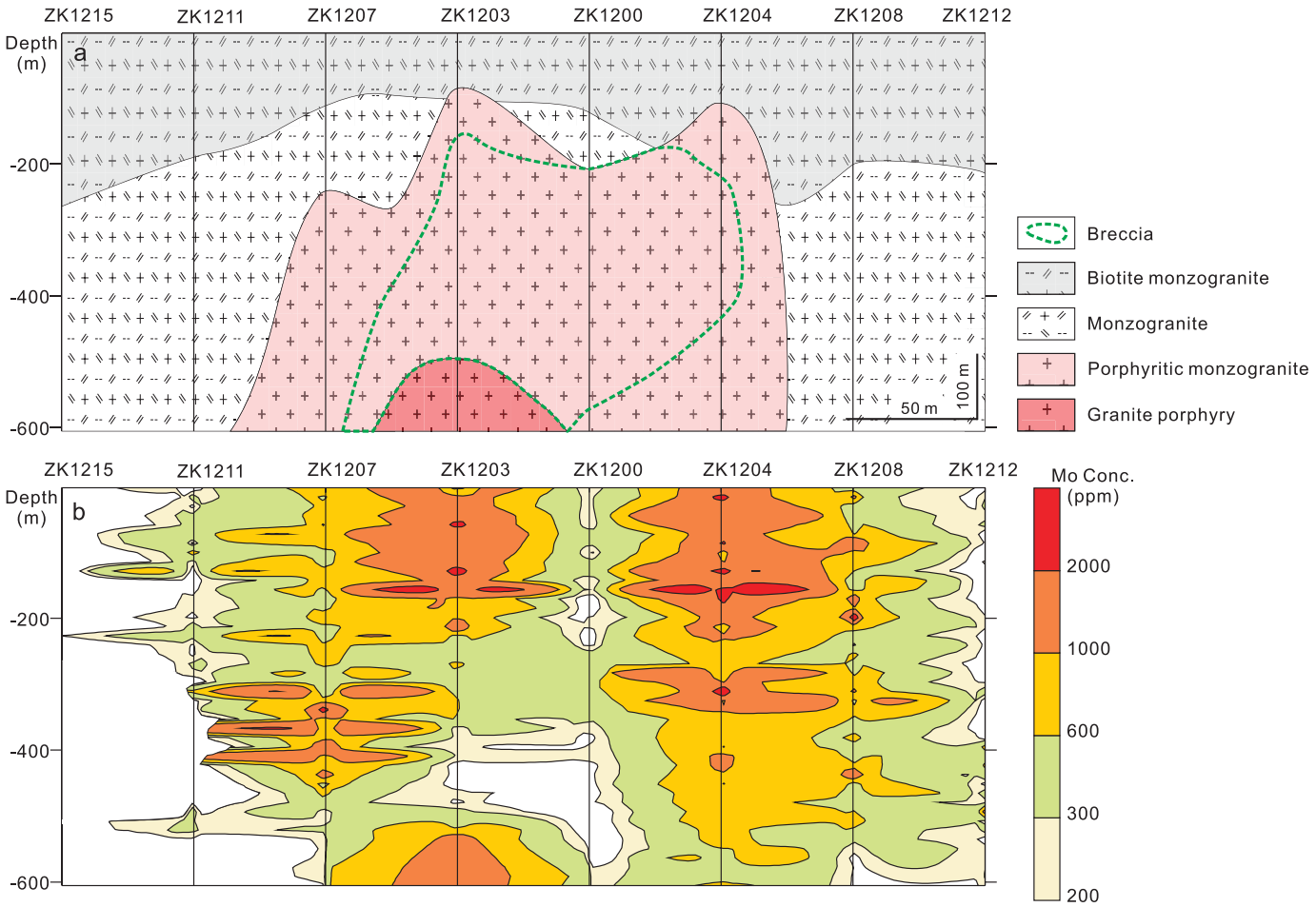

Fig. 5. Geologic cross section 12-12′ of the Luming deposit, showing (a) the crosscutting relationships of the Luming Intrusive Suite, and (b) the distribution of Mo grade. Assay data source: Yichun Luming Ming Co., LTD (unpub. data, 2010).

in the porphyritic monzogranite and granite porphyry units, with variable width (2–20 mm; Figs. 8, 9), and are crosscut by stage 4 D-type veins (Fig. 8g). They also occur within the biotite monzogranite and monzogranite units but are wider (up to 5 cm), and less abundant (Figs. 9c, 10a).

Stage 4 veins (D-type veins): Stage 4 D-type veins include quartz-molybdenite-pyrite ± chalcopyrite veins (i.e., D1 veins) and molybdenite veins (i.e., D2 veins), both with biotite- and feldspar-destructive alteration selvages. These subtype veins almost invariably cut the previously described vein types and intrusions (Figs. 8-11) and represent the volumetrically most significant molybdenite-bearing veins at Luming. D1 veins are typically 1–2.5 cm wide and are mainly composed of quartz and molybdenite with lesser amounts of pyrite. They are usually cut and offset by narrow D2 veins (1–1.5 mm in width), which consist of molybdenite with fine-grained sericite and chlorite selvages (Fig. 10e). However, abnormal vein crosscutting relationships, i.e., D2 veins cut by D1 veins, can also been observed (Fig. 10d). D1 and D2 veins are abundant within the biotite monzogranite and monzogranite units but are less abundant in the porphyritic monzogranite and granite porphyry units, coincident with an increase in Mo grade and a reduction in potassic alteration intensity (Table 2).

Stage 5 veins (D-type veins): Stage 5 veins (i.e., D3 veins) are composed of quartz, pyrite, and calcite, with sericite and chlorite halos. They are mainly hosted in the biotite monzogranite and monzogranite units (Figs. 10h, 12g, h). In some instances, D3 veins cut the pervasively altered porphyritic monzogranite unit (Fig. 11f) or the pervasively altered magmatic-hydrothermal breccias in the porphyritic monzogranite unit (Fig. 11e).

Stage 6 veins (D-type veins): Stage 6 veins (i.e., D4 veins), consisting of calcite, are mainly observed in the biotite monzogranite unit where they cut D2 veins (Fig. 10e). As shown in Figure 12i, quartz-pyrite veins (D3) are crosscut by calcite veins (D4), indicating D4 veins are the youngest vein sequence at Luming.

Magmatic-hydrothermal breccia body

In the mining area, drill cores to a depth of 600 m intersected a concealed, cylindrical magmatic-hydrothermal breccia body with horizontal dimensions of ~200 m and vertical extent of over 400 m (Figs. 3a-5a). It intrudes into the porphyritic monzogranite unit and is capped by the biotite monzogranite and monzogranite units. The breccia body is in turn crosscut by the porphyry granite and syenogranite units, suggesting that the two units were coeval with and/or postdated breccia body emplacement. Breccias from the breccia body are dominantly

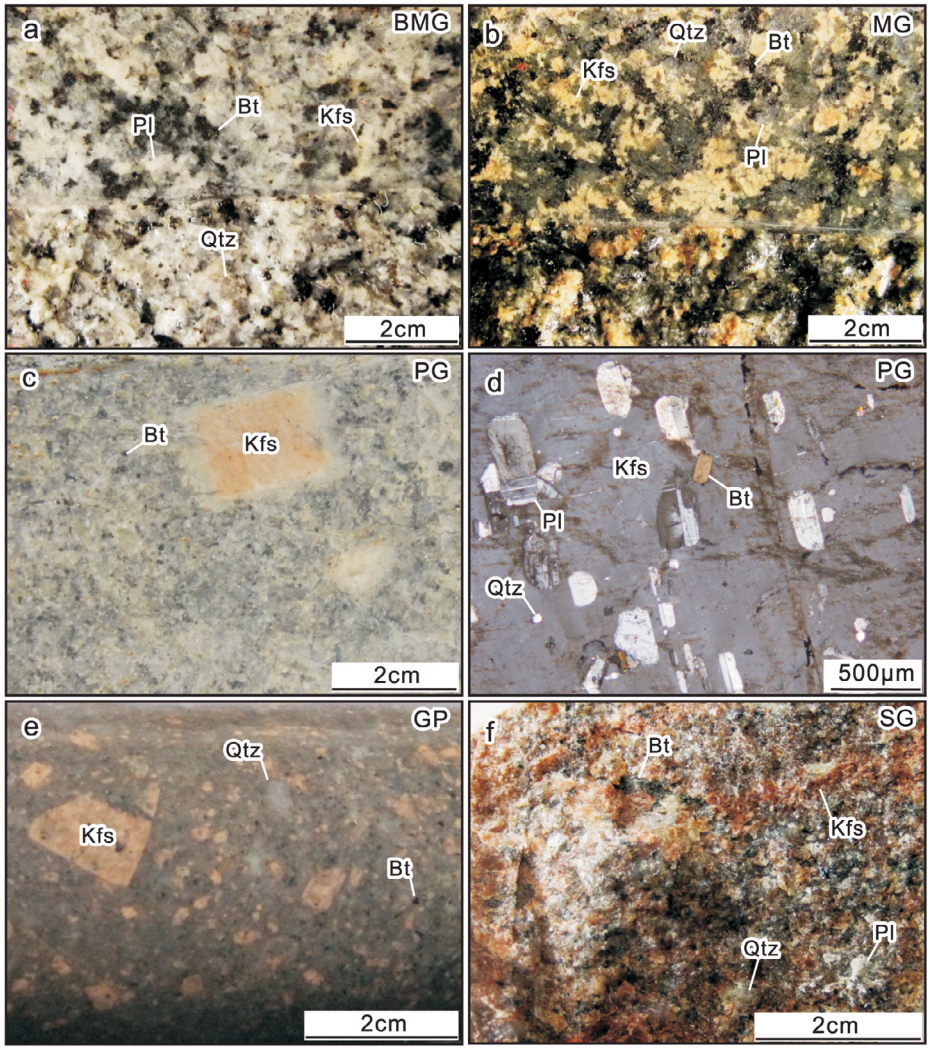

Fig. 6. Photographs and photomicrographs of the five intrusive units of the Luming Intrusive Suite. (a) Biotite monzogranite. (b) Monzogranite. (c) Porphyritic monzogranite. (d) Mineral inclusions consist of biotite, K-feldspar, plagioclase, and quartz hosted in alkali feldspar megaphenocryst of porphyritic monzogranite (cross-polarized light). (e) Granite porphyry. (f) Syenogranite. Abbreviations: BMG = biotite monzogranite, Bt = biotite, GP = granite porphyry, Kfs = K-feldspar, MG = monzogranite, PG = porphyritic monzogranite, Pl = plagioclase, Qtz = quartz, SG = syenogranite.

composed of porphyritic monzogranite clasts encased within veins ranging from quartz to quartz-molybdenite ± pyrite in composition (Fig. 11), with vein abundance decreasing with increasing depth. The biotite monzogranite and monzogranite have not been observed as clasts within the breccias. The porphyritic monzogranite clasts are angular and have jigsaw-fit texture, which preserves evidence of earlier stages of disseminated molybdenite mineralization that predate brecciation (Fig. 11c). Locally, the breccias also contain clasts of quartz-molybdenite fragments that represent earlier stages of mineralization (Fig. 11e).

Ore-grade zonation

At Luming, molybdenite is the only mineral present in economic abundances; other metals such as Cu, Pb, and Zn are insignificant. Within the overall deposit, Mo mineralization exhibits a surface dimension of approximately 1,900 × 1,700 m and generally extends from the surface to a depth of 100–600 m (Figs. 2b, 3–5). Moreover, the pattern of Mo mineralization (i.e., quartz-molybdenite ± pyrite and molybdenite ± pyrite) distribution is somewhat irregular and exhibits multiple zones of concentration as shown in cross sections of 00-00′, 04-04′, and 12-12′ (Figs. 3b-5b).

Generally, at shallow levels (≤200 m below the current ground surface), molybdenite mineralization with Mo grades higher than 0.06 wt % is abundant within the biotite monzogranite, monzogranite, and porphyritic monzogranite units (Figs. 3b-5b), especially in areas where the porphyritic monzogranite unit develops apophyses that intruded into the biotite monzogranite and monzogranite units. Peripheral to the porphyritic monzogranite units, Mo grade drops off gradually with increasing distance.

At intermediate levels (200–400 m below the current ground surface), molybdenite mineralization mainly occurs in the porphyritic monzogranite unit with highly variable Mo grade. The main portion of the porphyritic monzogranite unit at this level contains 0.03–0.06 wt % Mo. However, it locally contains zones, tens of meters thick, of high-grade mineral-

Table 2. Vein Types at the Luming Deposit (in relative age sequence, oldest at top)

Vein type	Mineral assemblage	Alteration halo	Thickness (mm)	Vein texture	Occurrence in the intrusive complex	Crosscutting relationships
EB	Bt	Kfs	<1	Sinuous, deformed	Rare in PG, GP, and SG	
A1	Qtz ± bt	None	1–5	Sinuous, linear, parallel-sided	Minor in PG and GP	Cut EB veins
A2	Qtz	Kfs	1–8	Linear, parallel-sided	Minor in PG, GP, and SG	Cut A1 veins
B	Qtz-mo	Kfs	3–50	Linear, parallel-sided	Some in PG, GP, and BMG	Cut A1 and A2 veins
D1	Qtz-mo ± py ± clp	Ser ± chl	10–25	Linear, parallel-sided	Abundant in BMG and MG, minor in PG and GP	Cut A1, A2, and B veins
D2	Mo	Ser ± chl	1–1.5	Linear, parallel-sided	Some in BMG and MG, minor in PG and GP	Cut A1, A2, B, and D1 veins
D3	Qtz-py ± cal	Ser ± chl	5–15	Linear, parallel-sided	Abundant in BMG and MG, rare in PG	Not observed
D4	Cal	Ser ± chl ± kln	1–10	Linear, parallel-sided	Some in BMG and MG	Cut D2 and D3 veins

Abbreviations: BMG = biotite monzogranite, Bt = biotite, Cal = calcite, Chl = chlorite, Clp = chalcopyrite, GP = granite porphyry, Kfs = K-feldspar, Kln = kaolinite, MG = monzogranite, Mo = molybdenite, PG = porphyritic monzogranite, Py = pyrite, Qtz = quartz, SG = syenogranite, Ser = sericite

ization (>0.06 wt % Mo). For example, ZK04-03 intersects an ~80-m-thick zone of abundant molybdenite-bearing veins with intensive potassic and phyllic alteration assayed at >0.06 wt % Mo (Fig. 3b, c).

At deeper levels (>400 m below the current ground surface), molybdenite mineralization mainly occurs in the porphyritic monzogranite, granite porphyry, and syenogranite units, but the Mo grade is generally lower than that encountered at shallower levels (Figs. 3b-5b). Although intrusive units at this level contain uneconomic Mo mineralization, grade decline across intrusive contacts is still obvious. For example, across the contact from the monzogranite to granite porphyry units revealed by drill core ZK04-06 (Fig. 3b), Mo grade declines from ~0.025 wt % to ~0.013 wt % (Yichun Luming Ming Co., LTD, unpub. data, 2010), whereas the volume of quartz veining and intensity of potassic alteration exhibit an opposing trend (Fig. 9c). A similar drop in Mo grade also occurs across the porphyritic monzogranite to syenogranite units at this level.

Alteration and zonation

We have identified four hydrothermal alteration types within the units of the Luming Intrusive Suite: potassic, phyllic, propylitic, and argillic. They are broadly centered on the intrusive complex consisting of porphyritic monzogranite, granite porphyry, and syenogranite units and typically form systematic zones transitioning from the center upward from potassic, phyllic, to argillic alteration (Fig. 3c) and grading marginally into weakly developed propylitic alteration. However, cyclical sequences of veining during the assembly of the Luming Intrusive Suite may have served to make alteration characteristics at Luming more complicated.

Potassic alteration is represented by the formation of K-feldspar envelopes along EB-, A-, or B-type veins (Figs. 8-10a, 12a-c). Hence, the intensity and zonation of potassic alteration vary with the abundance of these high-temperature veins within the different units of the Luming Intrusive Suite. Generally, potassic alteration is most intense within and around the porphyritic monzogranite unit (Fig. 3c) in which A- and B-type

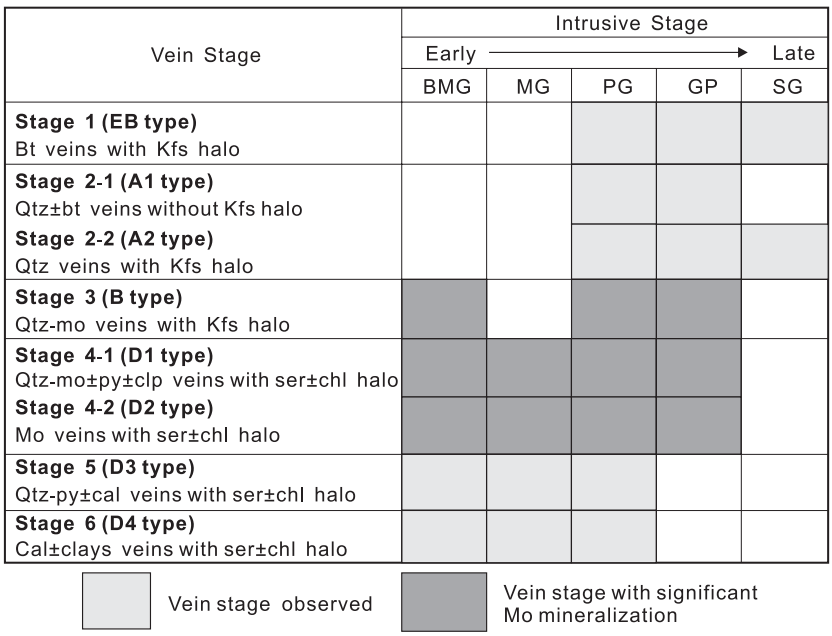

Fig. 7. Schematic diagram summarizing the vein stages observed in intrusions of the Luming Intrusive Suite. This diagram emphasizes that similar veining and alteration sequences are repeated in each synmineralization intrusion. Abbreviations: BMG = biotite monzogranite, Bt = biotite, Cal = calcite, Chl = chlorite, Clp = chalcopyrite, Fsp = feldspar, GP = granite porphyry, Hyd. = hydrothermal, Kfs = K-feldspar, Kln = kaolinite, MG = monzogranite, Mo = molybdenite, PG = porphyritic monzogranite, Pl = plagioclase, Pri. = primary, Py = pyrite, Qtz = quartz, Ser = sericite, SG = syenogranite.

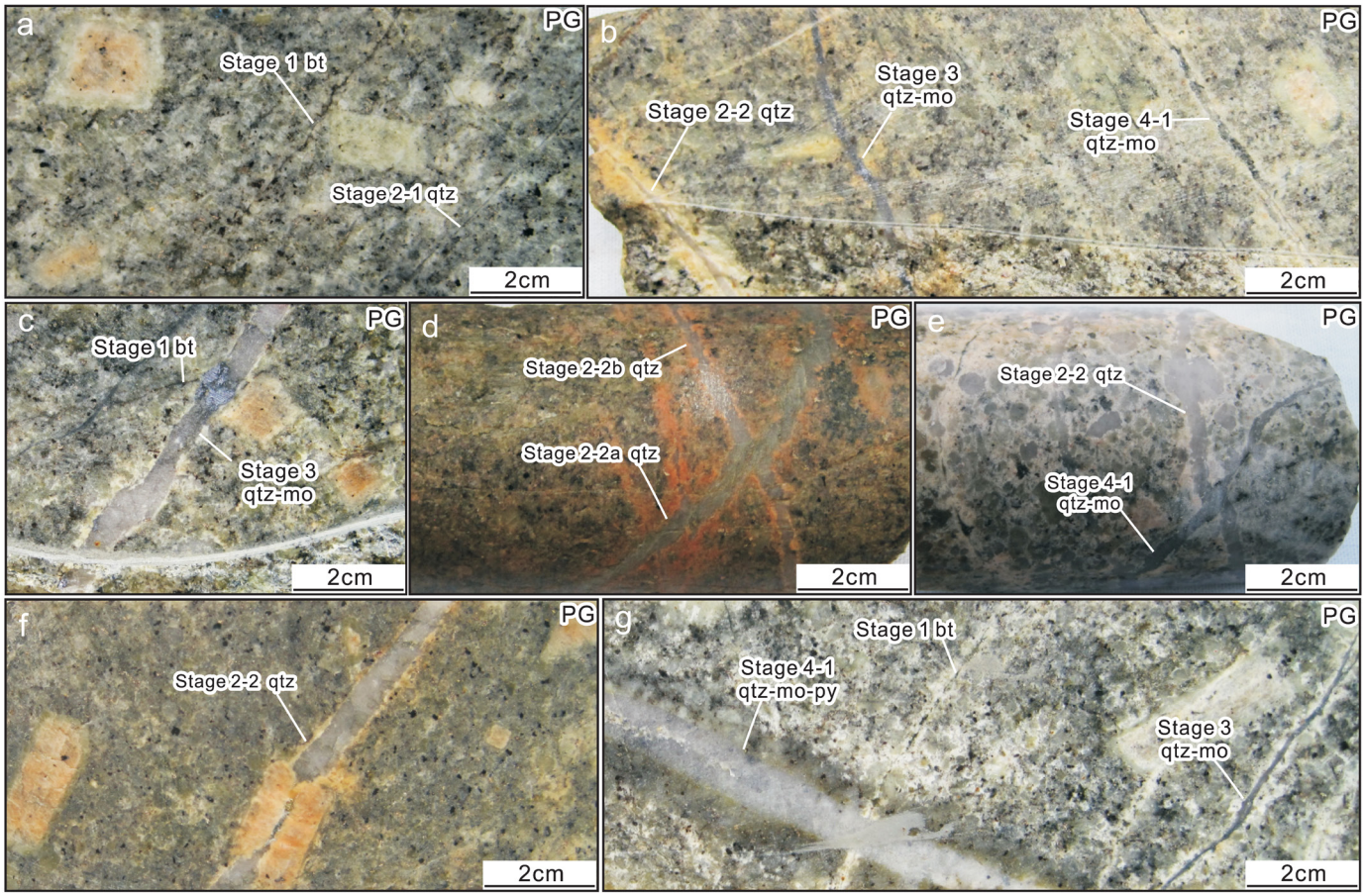

Fig. 8. Representative photographs of vein styles in the porphyritic monzogranite. (a) Porphyritic monzogranite cut by stage 1 biotite and stage 2 quartz veins. (b) Porphyritic monzogranite cut by stage 2 quartz-K-feldspar, stage 3 quartz-molybdenite, and stage 4 quartz-molybdenite veins. (c) Stage 1 biotite vein in porphyritic monzogranite cut by stage 3 quartz-molybdenite vein. (d) Mutual crosscutting relationship of stage 2 quartz-K-feldspar veins in porphyritic monzogranite. (e) Stage 2 quartz vein in porphyritic monzogranite cut by stage 4 quartz-molybdenite vein. (f) Porphyritic monzogranite cut by stage 2 quartz-K-feldspar vein. (g) Porphyritic monzogranite cut by stage 1 biotite and stage 3 quartz-molybdenite veins, in turn cut by stage 4 quartz-molybdenite-pyrite vein. Abbreviations: Bt = biotite, Mo = molybdenite, PG = porphyritic monzogranite, Py = pyrite, Qtz = quartz.

veins are well developed (Figs. 8, 11). Such alteration becomes less intense in the granite porphyry and syenogranite units because of the lower abundance of high-temperature veins (Fig. 9). The potassic alteration displays a spatial association with Mo mineralization; however, only an estimated 10–15% of Mo was introduced during this alteration stage based on modal abundance estimates of Mo during core logging.

In the magmatic-hydrothermal breccia body, a zone of pervasive potassic alteration extending vertically up to 400 m is observed in which A- and B-type veins constitute >15 vol % of the rock (Figs. 3c, 11). Distinguishing characteristics of this zone are the pervasive red color of affected rocks, intense silicification, the relics of K-feldspar and quartz phenocrysts, and quartz-molybdenite fragments (Figs. 11, 12d, e). In this zone, primary rock-forming silicates of the porphyritic monzogranite have been replaced almost entirely by quartz and K-feldspar and cut by later A- and B-type veins. Chlorite-sericite alteration, giving rise to distinctive pale-green rocks, is also developed in this zone, where it overprints and partially destroys the preexisting potassic assemblages with sericite, pyrite, and molybdenite (Fig. 11b, e, f). Molybdenum grade in this zone may increase as indicated by the introduction of molybdenite-bearing B- and D-type veins (e.g., Fig. 11a-d).

Phyllic alteration is characterized by the replacement of all rock minerals by fine-grained sericite, quartz, and chlorite accompanied by a small percentage of disseminated pyrite along D1- and D2-type veins (Figs. 8b-g, 10b-g, 12f, g). It affects all units of the Luming Intrusive Suite, but the intensity varies with the abundance of D1- and D2-type veins. This type of alteration tends to be more pervasive throughout the biotite monzogranite and monzogranite units and overprints the propylitic alteration (e.g., Fig. 10e), forming an envelope surrounding the potassic alteration zone (Fig. 3c). Phyllic alteration also extends to greater depth as a late, low-temperature overprint atop the potassic zone, as revealed by drill cores ZK04-03, ZK04-00, ZK04-04, and ZK04-06 (Fig. 3a). Phyllic alteration is invariably associated with molybdenite mineralization; perhaps as much as 80% of the molybdenite was deposited during this alteration episode, based on modal abundance estimates of Mo during core logging.

Propylitic alteration consists of a sericite-chlorite-pyrite ± calcite assemblage and is pervasive in the biotite monzogran-

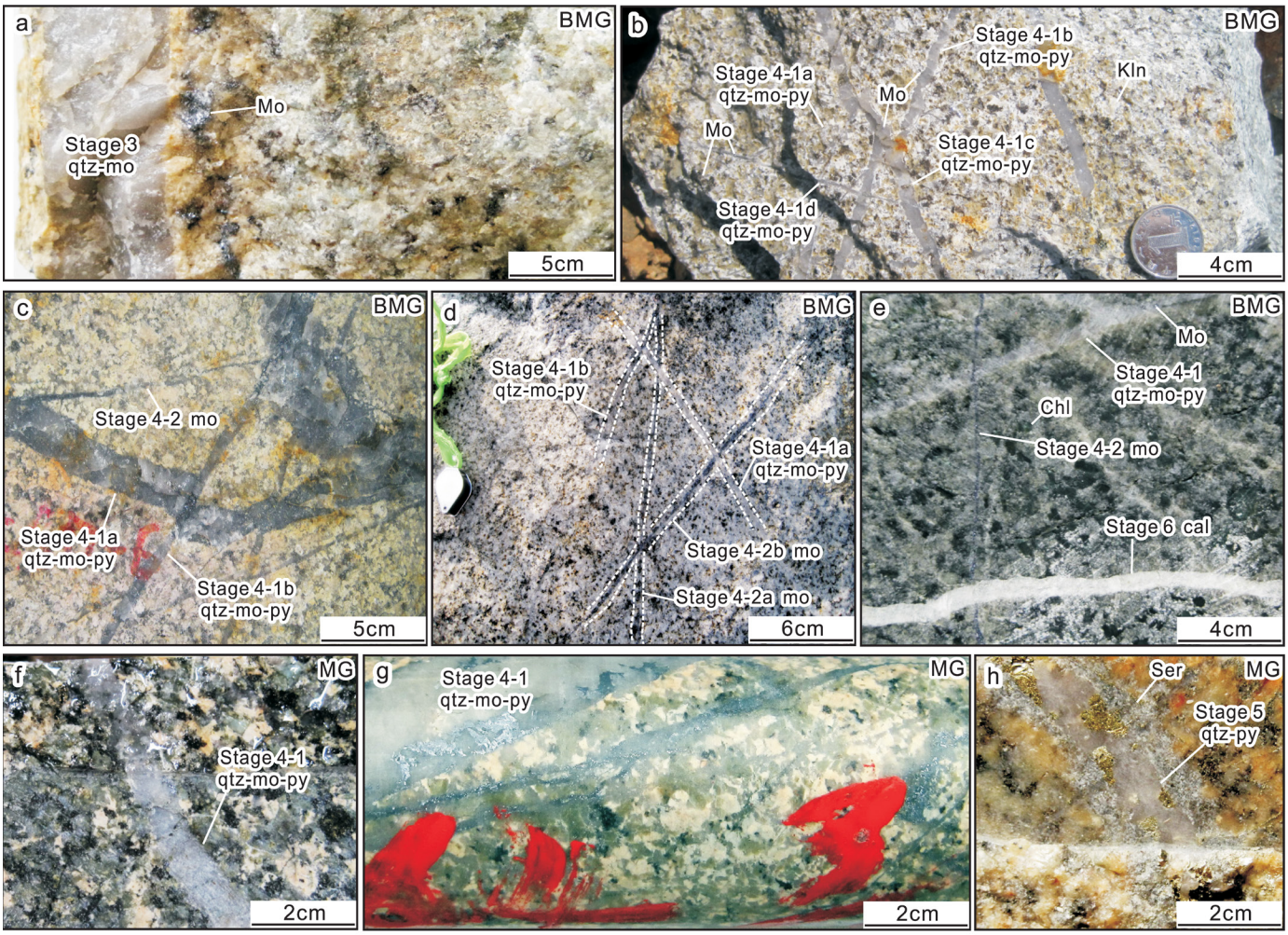

Fig. 10. Representative photographs of vein styles in the biotite monzogranite and monzogranite. (a) Stage 3 quartz-molybdenite vein with disseminated molybdenite occurring near the vein margin. (b) Mutual crosscutting relationships of stage 4 quartz-molybdenite-pyrite vein in biotite monzogranite, indicating multiple stages of mineralization. (c) Stage 4 quartz-molybdenite-pyrite vein in biotite monzogranite cuts stage 4 molybdenite vein, in turn cut by later stage 4 quartz-molybdenite-pyrite vein. (d) Stage 4 molybdenite veins in biotite monzogranite cut by two generations of stage 4 quartz-molybdenite-pyrite vein. (e) Stage 4 quartz-molybdenite-pyrite vein in biotite monzogranite cut by stage 4 molybdenite vein, in turn cut by stage 6 calcite vein. (f, g) Stage 4 quartz-molybdenite-pyrite vein in monzogranite. (h) Stage 4 quartz-pyrite vein in monzogranite. Abbreviations: BMG = biotite monzogranite, Cal = calcite, Kln = kaolinite, MG = monzogranite, Mo = molybdenite, Py = pyrite, Qtz = quartz, Ser = sericite.

ite and monzogranite units peripheral to the potassic zone (Fig. 3). It occurs as quartz-pyrite ± calcite vein (D3-type vein) halos (e.g., Figs. 10h, 11f, 12h) or as pervasive replacements in which feldspar and biotite have been replaced by fine-grained sericite and chlorite with disseminated pyrite (e.g., Fig. 10e). The propylitic alteration was overprinted by phyllic alteration (Fig. 10e), suggesting that it was probably contemporaneous with potassic alteration.

Argillic alteration consisting of kaolinite, quartz, and hematite is observed at the shallow level of the biotite monzogranite and monzogranite units (Figs. 3c, 10b, c). It overprints and partly dissolves earlier phyllic alteration, which in extreme cases results in vuggy quartz (Fig. 10b). Calcite veins (D4-type veins), which are the youngest vein type at Luming, are inferred to be associated with argillic alteration (Figs. 10e, 12i).

U-Pb geochronology of the Luming Intrusive Suite

The zircon U-Pb dating results of individual units are listed in Appendix Table A3 and graphically presented in Figure 13. Uncertainties on individual analyses and weighted mean $^{206}Pb/^{238}U$ ages are reported at the 2σ level.

Zircon grains from the biotite monzogranite unit show weak euhedral oscillatory zoning in CL images. They are commonly 100–150 μm in length and 50–100 μm in width, with aspect ratios between 1.0 and 2.0 and contain variable U and Th concentrations ranging from 168 to 2,542 ppm and 100 to 1,344 ppm, respectively (corresponding to Th/U values of 0.33–0.95). The 28 zircon grains analyzed here are concordant, yielding $^{206}Pb/^{238}U$ ages between 188 and 186 Ma and a weighted mean $^{206}Pb/^{238}U$ age of 187.5 ± 2.8 Ma (2σ; MSWD = 0.02; Fig. 13a).

Zircons of the monzogranite unit are euhedral, typically 100–200 μm in length and 50–100 μm in width, showing fine-scale

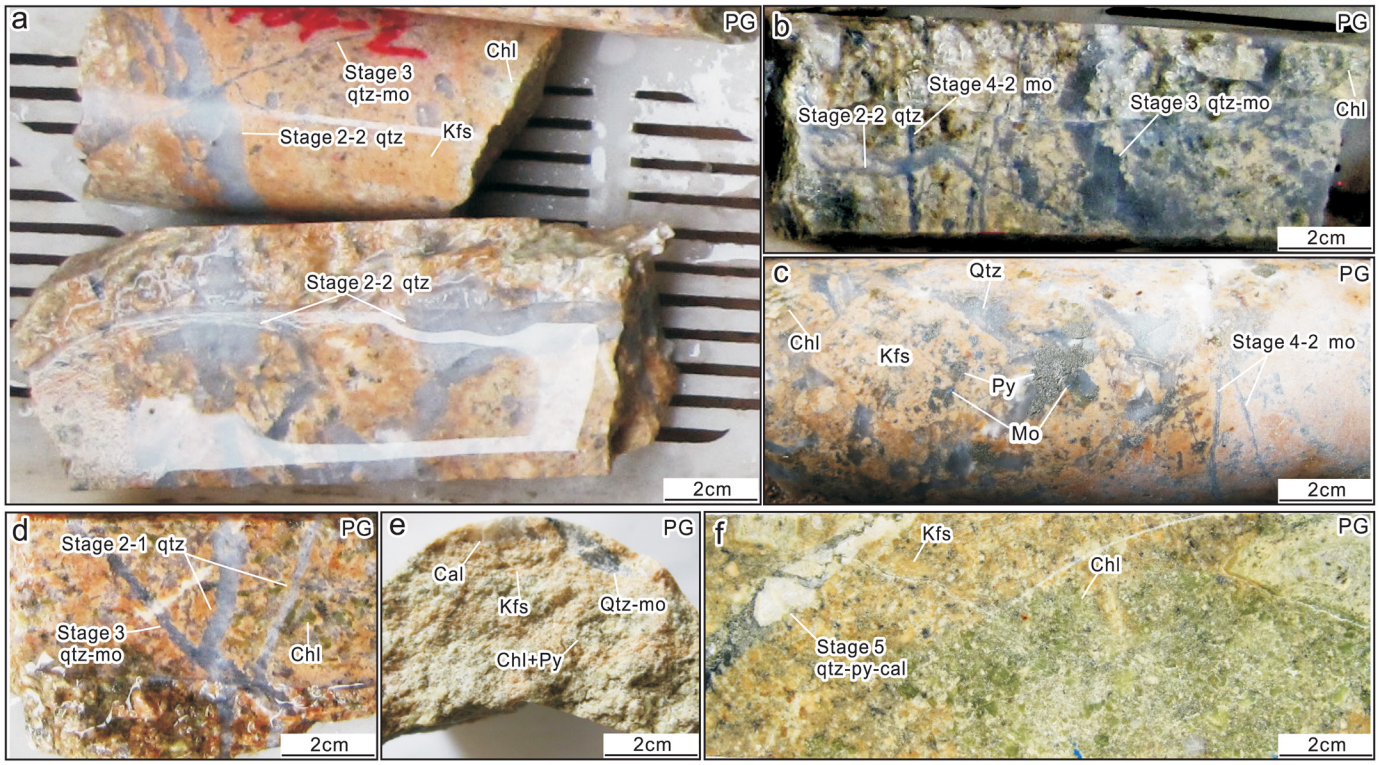

Fig. 11. Representative photographs of the pervasively altered porphyritic monzogranite and hydrothermal breccias. (a) Intensely potassic-altered porphyritic monzogranite cut by stage 2 quartz-K-feldspar vein that is in turn cut by stage 3 quartz-molybdenite vein (upper part), and stage 2 quartz-K-feldspar vein cutting intensely altered breccia of porphyritic monzogranite (lower part). (b) Intensely altered porphyritic monzogranite cut by stage 3 quartz-molybdenite and stage 4 molybdenite veins that are in turn cut by stage 2 quartz-K-feldspar vein. (c) Mineralized breccia containing clasts of porphyritic monzogranite with disseminated molybdenite that are in turn cemented by matrix of quartz, molybdenite, and pyrite and truncated by molybdenite stockworks, indicating that porphyritic monzogranite was mineralized prior to the incorporation of the clasts in the breccia. (d) Pervasively altered porphyritic monzogranite cut by stage 2 quartz vein, in turn cut by stage 3 quartz-molybdenite vein. (e) Intensely altered breccia of porphyritic monzogranite with fragment of quartz-molybdenite overprinted by late-stage phyllic alteration. (f) Pervasively altered porphyritic monzogranite heavily overprinted by late-stage phyllic alteration that is in turn cut by stage 5 quartz-pyrite-calcite vein. Abbreviations: Cal = calcite, Chl = chlorite, Clp = chalcopyrite, Kfs = K-feldspar, Mo = molybdenite, PG = porphyritic monzogranite, Py = pyrite, Qtz = quartz.

oscillatory growth zoning overprinted by strong sector zoning. They have 270–2,729 ppm U and 169–2,028 ppm Th, with Th/U ratios of 0.51–0.75. The 18 analyzed zircon grains form a clustered group on the U-Pb concordia and yield a weighted mean $^{206}Pb/^{238}U$ age of 186.5 ± 3.6 Ma (2σ; MSWD = 0.02; Fig. 13b).

Zircons from the porphyritic monzogranite unit are typically 150–300 μm in length and ~100 μm in width, showing the development of euhedral oscillatory zoning. They have variable U (1,233–4,260 ppm) and Th (364–3,135) contents, with Th/U ratios of 0.30–0.80. The 20 analyses are concordant and have a weighted mean $^{206}Pb/^{238}U$ age of 178.6 ± 2.2 Ma (2σ; MSWD = 0.06; Fig. 13c).

Zircons of the granite porphyry unit are euhedral, elongate, and oscillatory zoned in CL images, with lengths of 150–300 μm and widths of ~100 μm. They have 212–3,156 ppm U and 82–2,361 ppm Th, with variable Th/U ratios of 0.32–1.42. Individual zircon grains (n = 19) yield $^{206}Pb/^{238}U$ ages ranging from 178 to 176 Ma and a weighted mean $^{206}Pb/^{238}U$ age of 177.4 ± 3.0 Ma (2σ; MSWD = 0.02; Fig. 13d).

Zircon grains from the syenogranite unit are euhedral, 100–350 μm in length, and ~100 μm in width, showing similar internal CL patterns as zircons from the porphyritic monzogranite and granite porphyry units. They have variable U (143–1,237 ppm) and Th (69–630 ppm), with Th/U ratios of 0.35–0.70. The 20 analyzed zircon grains are concordant and yield a weighted mean $^{206}Pb/^{238}U$ age of 175.6 ± 3.0 Ma (2σ; MSWD = 0.01; Fig. 13e).

$^{40}Ar/^{39}Ar$ geochronology

Step-heating $^{40}Ar/^{39}Ar$ dating results for hydrothermal biotite collected from drill core sample of the syenogranite unit are presented in Appendix Table A4 and illustrated in Figure 13f. Uncertainties on individual step-heating analyses and plateau age are reported at the 2σ level. The ^{39}Ar release profile shows a slight disturbance in the low-temperature steps (700°–800°C) but produced a plateau age of 174.7 ± 1.1 Ma (2σ, MSWD = 0.30) between steps 3 and 12, accounting for 96.2% of the ^{39}Ar released. In the inverse isochron plot (App. Table A4), an initial $^{40}Ar/^{36}Ar$ ratio of 297 ± 35 is obtained, which overlaps with the atmospheric value (298.56 ± 0.31; Lee et al., 2006).

Melt inclusion compositions

Despite extensive detailed observations, only phenocrysts of quartz from the granite porphyry unit of the Luming Intrusive

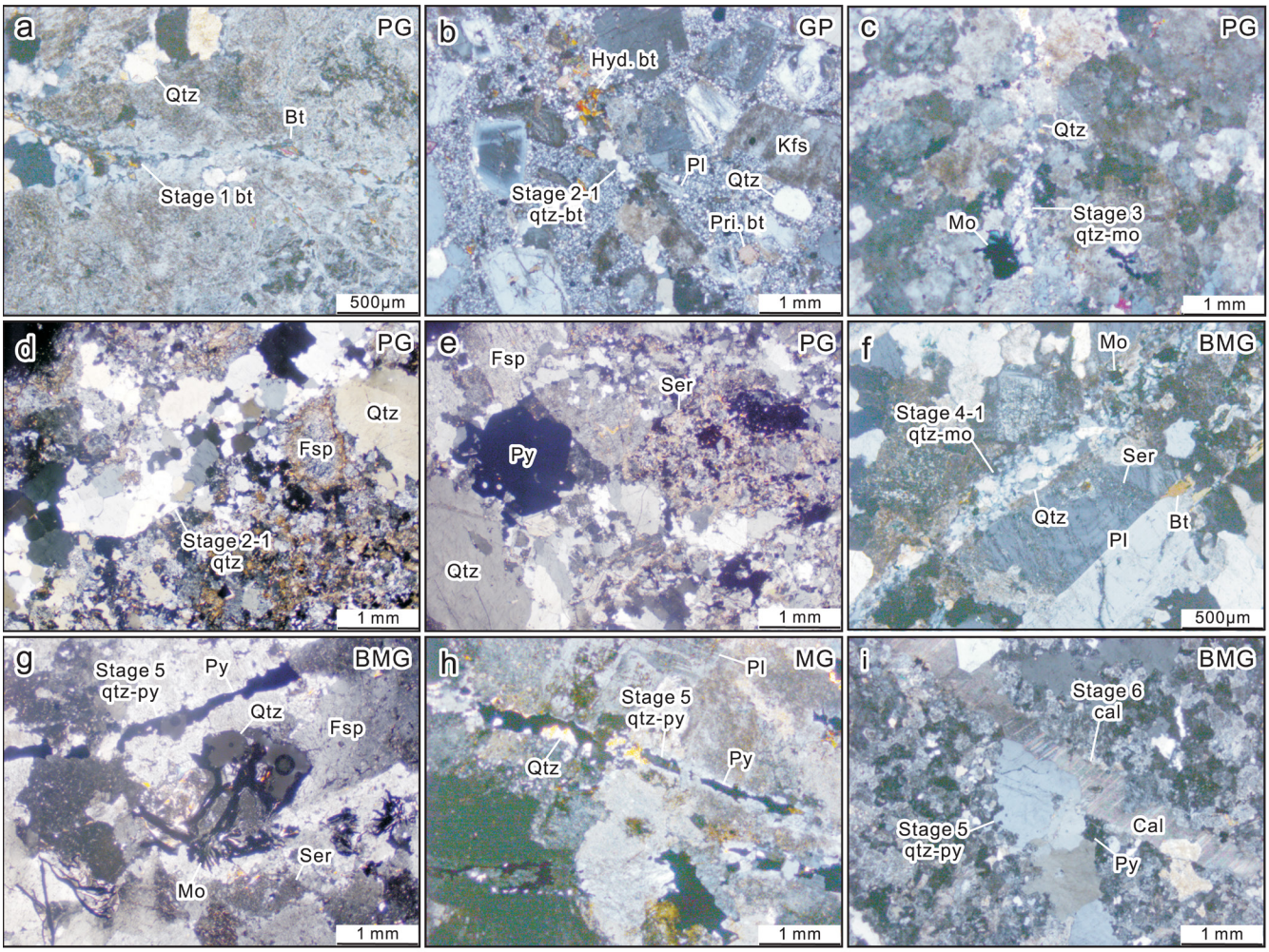

Fig. 12. Photomicrographs of alteration and related vein stage at Luming. (a) Stage 1 biotite vein with fine-grained K-feldspar halo in porphyritic monzogranite. (b) Stage 2 quartz-biotite vein in granite porphyry. (c) Stage 3 quartz-molybdenite vein with fine-grained K-feldspar halo in porphyritic monzogranite. (d) Pervasively altered porphyritic monzogranite cut by stage 2 quartz vein. (e) Pervasively altered porphyritic monzogranite overprinted by phyllic alteration. (f) Stage 4 quartz-molybdenite vein with alteration halos of sericite in biotite monzogranite. (g) Molybdenite mineralized biotite monzogranite cut by stage 5 quartz-pyrite vein. (h) Fine-grained sericite halo around stage 5 quartz-pyrite vein in monzogranite. (i) Stage 6 calcite vein cutting stage 5 quartz-pyrite vein in biotite monzogranite. All photos were taken under cross-polarized light. Abbreviations: BMG = biotite monzogranite, Bt = biotite, Cal = calcite, Fsp = feldspar, GP = granite porphyry, Hyd. = hydrothermal, Kfs = K-feldspar, MG = monzogranite, Mo = molybdenite, PG = porphyritic monzogranite, Pl = plagioclase, Pri. = primary, Py = pyrite, Qtz = quartz, Ser = sericite.

Suite contained workable melt inclusions for in situ major and trace element analysis (App. Fig. A1). In addition, owing to the poor preservation state of the melt inclusions in the granite porphyry samples, only limited crystallized melt inclusions (eight melt inclusions) were analyzed by LA-ICP-MS. Uncertainties associated with these analyses are estimated at 5–7%, except for elements close to the detection limit (e.g., Sn, Bi, Cu, and Li). The analyzed melt inclusions are trachydacite in composition (SiO_2 = 70.09–74.68 wt %; Na_2O = 4.26–7.16 wt %; K_2O = 6.17–9.64 wt %) and contain 56–223 ppm Rb and 1–3 ppm Cs (App. Table A5). Molybdenum concentrations in the melt inclusions were <4 ppm (Fig. 14). It is important to note that, although the Mo melt inclusion data obtained in the present study are limited, the data agree with results obtained from subduction-related porphyry Mo deposits (Lerchbaumer and Audétat, 2013, and references therein; Ouyang et al., 2020), suggesting the data presented in this study are representative of the melt inclusions as a whole.

Discussion

Timing of magmatism and mineralization at Luming

Previous research reported variable zircon U-Pb weighted mean $^{206}Pb/^{238}U$ ages of 201.1 ± 7.8 to 194.8 ± 1.4 Ma (2σ) for the biotite monzogranite unit by SHRIMP and LA-ICP-MS methods (Shao et al., 2012; Xi et al., 2018), which are older than the weighted mean $^{206}Pb/^{238}U$ age of 187.5 ± 2.8 Ma (2σ) obtained in this study (Fig. 15). Given that the weighted mean $^{206}Pb/^{238}U$ age of 194.8 ± 1.4 Ma reported by Xi et al. (2018) has an uncertainty similar to that of our study, it likely represents a distinct intrusive unit that has not been dated in the present study. However, it still does not discount the potential

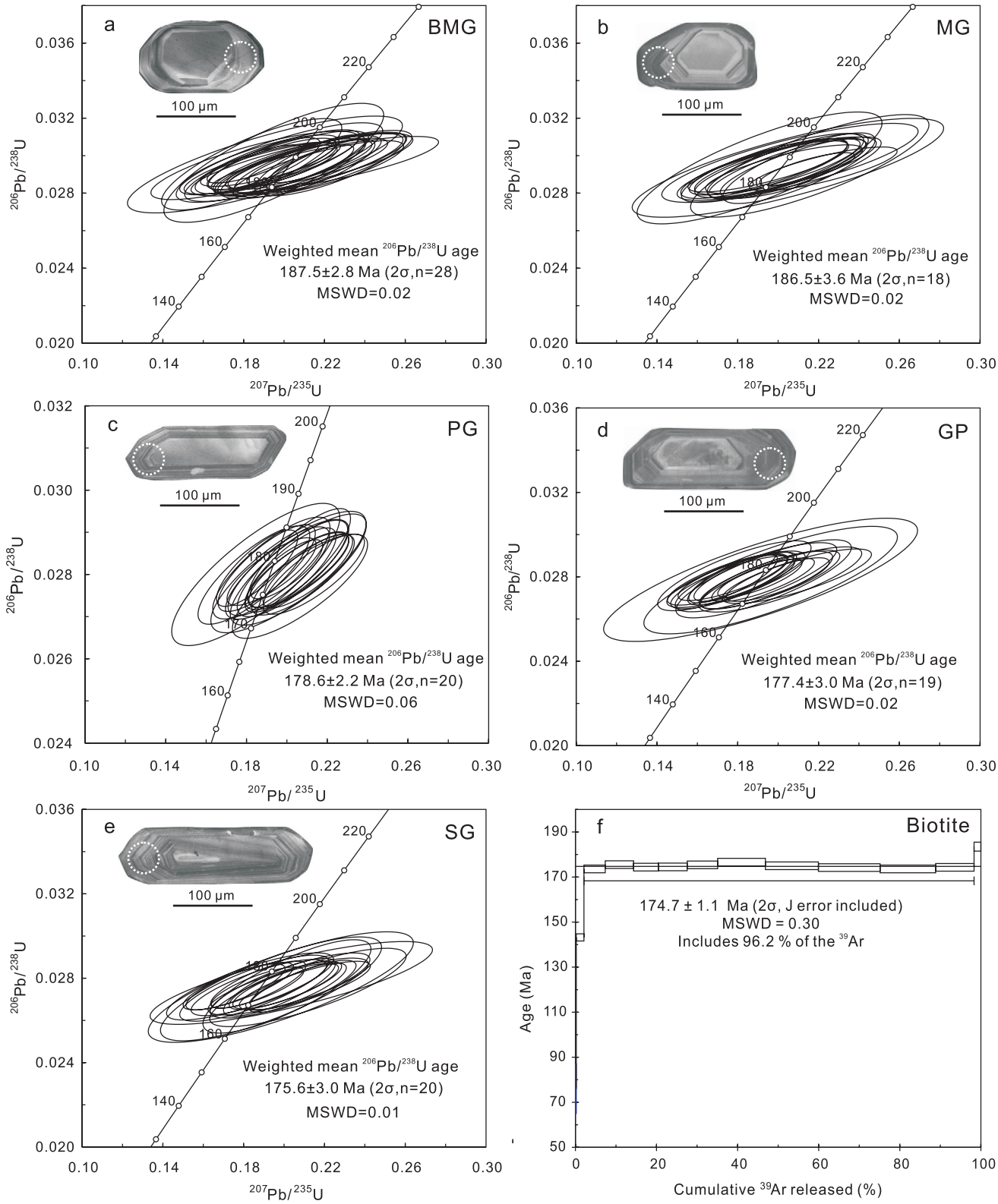

Fig. 13. Zircon U-Pb concordant diagrams for samples of (a) biotite monzogranite (BMG), (b) monzogranite (MG), (c) porphyritic monzogranite (PG), (d) granite porphyry (GP), and (e) syenogranite (SG), and (f) $^{40}Ar/^{39}Ar$ data of hydrothermal biotite from the Luming deposit. Also shown are the cathodoluminescence (CL) images of the zircon grains from individual intrusive units and the analytical spots. MSWD = mean square of weighted deviates.

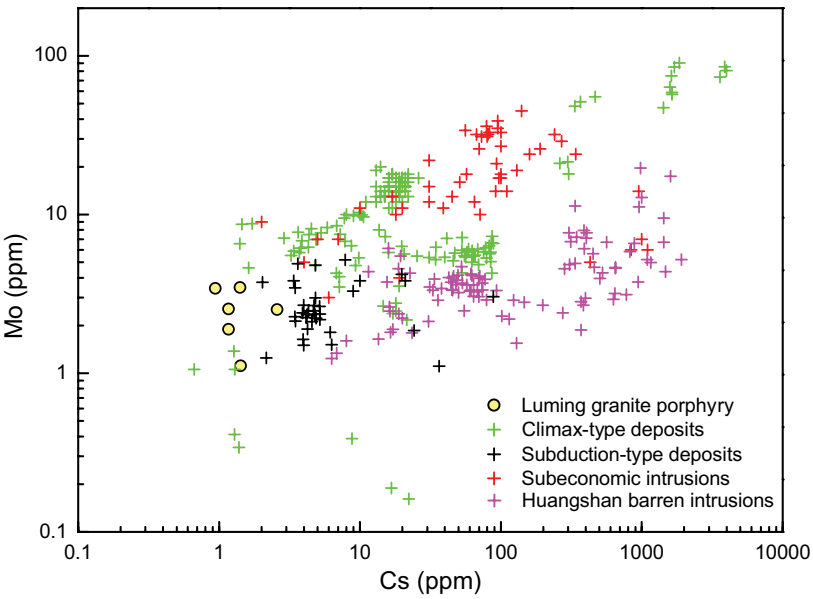

Fig. 14. Cesium versus Mo concentration in melt inclusions analyzed in the present study. The Cs and Mo concentrations in melt inclusions analyzed from Climax-type porphyry Mo deposits (Audétat, 2015; Audétat and Li, 2017; Zhang and Audétat, 2017), subeconomic occurrences with affinity to Climax-type deposits (Lerchbaumer and Audétat, 2013), subduction-type porphyry Mo deposits (Ouyang et al., 2020), and Huangshan barren felsic pluton (Zhang and Audétat, 2018) are shown for comparison.

for technical differences and interlaboratory bias in analysis as shown in studies of Li et al. (2017) and Cao et al. (2019). For the $^{206}Pb/^{238}U$ ages reported by Shao et al. (2012), as their uncertainties are large (2σ = 7.6–20.6; Fig. 15), the observed $^{206}Pb/^{238}U$ age dispersion (215.8–170.6 Ma; Fig. 15) and much older weighted mean $^{206}Pb/^{238}U$ age (201.1 ± 7.8 Ma) more likely reflect analytical problems (e.g., inheritance by analyzing cores and rims of zircon grains; Miller et al., 2007).

Our new LA-ICP-MS zircon U-Pb $^{206}Pb/^{238}U$ data show that the intrusion age of the monzogranite unit is 186.5 ± 3.6 Ma (2σ). This age is comparable to the zircon U-Pb weighted mean $^{206}Pb/^{238}U$ age of 187.1 ± 2.4 Ma (2σ) reported by Tan et al. (2012) for the same unit and overlaps within the 2σ uncertainty with the weighted mean $^{206}Pb/^{238}U$ age of the biotite monzogranite unit obtained in this study (Fig. 15). These two new weighted mean $^{206}Pb/^{238}U$ ages constrain the intrusion ages of the biotite monzogranite and monzogranite units within the range of 187.5 ± 2.8 to 186.5 ± 3.6 Ma, providing permissive evidence that they are cogenetic at the available temporal resolution.

The LA-ICP-MS zircon U-Pb weighted mean $^{206}Pb/^{238}U$ age of the porphyritic monzogranite unit obtained in this study is 178.6 ± 2.2 Ma (2σ). This date is comparable to the previously reported weighted mean $^{206}Pb/^{238}U$ age of 176.2 ± 4.2 Ma (2σ) for the same unit given by Xi et al. (2018) and overlaps within the 2σ uncertainties with the weighted mean $^{206}Pb/^{238}U$ ages of the granite porphyry and syenogranite units of 177.4 ± 3.0 (2σ) and 175.6 ± 3.0 Ma (2σ), respectively (Fig. 15). These three new ages constrain the intrusion ages of the porphyritic monzogranite, granite porphyry, and syenogranite units within a temporally unresolvable range between 178.6 ± 2.2 and 175.6 ± 3.0 Ma.

As shown in Appendix Table A2, the timing of mineralization at Luming has been constrained by ID-ICP-MS molybdenite Re-Os dating in many previous studies, which yielded model ages varying from 185.9 ± 1.9 to 176.0 ± 2.4 Ma (2σ; Tan et al., 2012; Hu et al., 2014; Liu et al., 2014; Sun et al., 2014, Cheng et al., 2015). However, the unclear textural context of the dated molybdenite and analyzed standards, coupled with interlaboratory bias in molybdenite Re-Os dating, raises doubt on the significance of these ages. In the present study, molybdenite Re-Os age data obtained by Tan et al. (2012), Hu et al. (2014), and Liu et al. (2014) are selected objectively because these dates were acquired in the same lab, using the same isotopic tracer and decay constant value, and thus can be directly compared at the level of their analytical uncertainties (Chiaradia et al., 2013). The selected 23 dates show molybdenite Re-Os model ages between 180.0 ± 2.6 and 177.0 ± 2.9 Ma and yield a mean age of 178.1 ± 2.7 (2σ; Fig. 15). These ages, combined with the $^{40}Ar/^{39}Ar$ plateau age of 174.7 ± 1.1 Ma (2σ) of hydrothermal biotite selected from EB-type veins hosted in the syenogranite unit, constrain the mineralization age at Luming within the range of 178.1 ± 2.7 to 174.7 ± 1.1 Ma.

Notably, the 2σ uncertainties of the data obtained in this and previous studies by using LA-ICP-MS zircon (1.2–1.9%; equivalent to absolute uncertainty of 2.2–3.6 m.y.; App. Table A3), MC noble gas mass spectrometer hydrothermal biotite (0.6%; equivalent to absolute uncertainties of 1.1 m.y.; App. Table A4), and ID-ICP-MS molybdenite (1.4 –1.9%; equivalent to absolute uncertainties of 2.5–3.3 m.y.; App. Table A2) methods are greater than the timescales of a single pulse of intrusive event and of magmatic-hydrothermal activity in porphyry systems (tens of thousands of years; Chiaradia et al., 2013, and references therein). To more precisely and accurately constrain the timing of magmatism and mineralization, further studies using high-precision chemical abrasion-isotope dilution-thermal ionization mass spectrometry (CA-ID-TIMS) U-Pb zircon and isotope dilution-negative thermal ionization mass spectrometry (ID-NTIMS) Re-Os molybdenite analysis are needed (e.g., Chelle-Michou et al., 2015; Li et al., 2017; Gaynor et al., 2019a). However, the ages presented in this study provide first-order constraints on the timing of magmatism and mineralization in the Luming deposit.

Intrusions responsible for the Luming porphyry Mo mineralization

Our detailed core logging data show that the Luming Intrusive Suite is composed of five major, successive intrusive

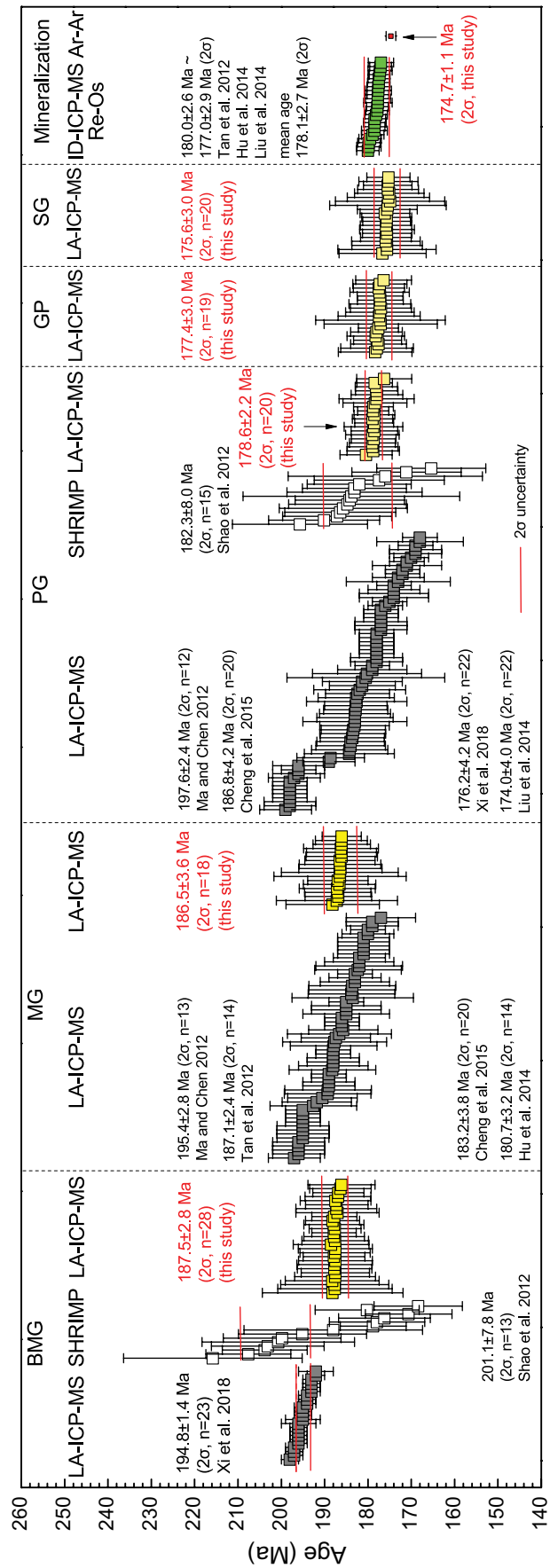

Fig. 15. Geologic time frame of the magmatic-hydrothermal events at Luming constrained by crosscutting relationships, LA-ICP-MS zircon U-Pb $^{206}Pb/^{238}U$ (yellow box) and hydrothermal biotite $^{40}Ar/^{39}Ar$ plateau (red box) ages of this study, and ID-ICP-MS molybdenite Re-Os model ages from previous studies (green box). See text for discussion. Only molybdenite Re-Os ages from Tan et al. (2012), Hu et al. (2014), and Liu et al. (2014) are selected, as these dates were acquired in the same lab and with the same isotopic tracer and decay constant value. For comparison, SHRIMP (white box) and LA-ICP-MS (gray box) zircon U-Pb $^{206}Pb/^{238}U$ ages from previous studies (Ma and Chen, 2012; Shao et al., 2012; Hu et al., 2014; Liu et al., 2012; Cheng et al., 2015; Xi et al., 2018) are shown. Detailed dates are provided in Appendix Tables A1 through A4. Vertical bar height is 2σ analytical uncertainty for all data. Abbreviations: BMG = biotite monzogranite, GP = granite porphyry, ID = isotope dilution, LA-ICP-MS = laser ablation-inductively coupled plasma-mass spectrometry, MG = monzogranite, PG = porphyritic monzogranite, SG = syenogranite.

units of the biotite monzogranite, monzogranite, porphyritic monzogranite, granite porphyry, and syenogranite. The former two units have been ascribed to the causative intrusions for Mo mineralization at Luming by former studies based on their pervasive Mo mineralization with intense sericite ± chlorite alteration (e.g., Shi et al., 2007; Shao et al., 2012; Tan et al., 2012; Hu et al., 2014; Sun et al., 2014). The fact that the biotite monzogranite and monzogranite units are of plutonic dimensions (>6.5 km^3; exposed over an area of >2.7 × 2.4 km and assuming a minimum thickness of 1.0 km; Figs. 2–5) and the lack of high-temperature EB- and A-type veins (Fig. 7) indicate that they are more likely premineralization intrusions. This interpretation is supported by the zircon U-Pb weighted mean $^{206}Pb/^{238}U$ ages of the biotite monzogranite and monzogranite units (187.5 ± 2.8–186.5 ± 3.6 Ma; Fig. 15), which are earlier than the mean molybdenite Re-Os model and hydrothermal biotite $^{40}Ar/^{39}Ar$ plateau ages (178.1 ± 2.7–174.7 ± 1.1 Ma; Fig. 15) by approximately 8.4–12.8 m.y.

As shown in Figures 3 through 5, the porphyritic monzogranite, granite porphyry, and syenogranite units are progressively smaller in volume and more deeply emplaced into the premineralization plutonic biotite monzogranite and monzogranite units as stock- and dike-like intrusions. Such spatial and temporal relationships between the earlier barren plutonic and later small intrusions have been recognized at a number of other porphyry deposits, including the Bingham, Yerington, Climax, Henderson, Questa, and Endako deposits, in which the later intrusions were evidenced to be syn- or postmineralization (Carten et al., 1988; Bookstrom, 1989; Dilles et al., 2000; Villeneuve et al., 2001; Redmond and Einaudi, 2010; Gaynor et al., 2019a, b). Our geochronology data show that the zircon U-Pb weighted mean $^{206}Pb/^{238}U$ ages of the porphyritic monzogranite, granite porphyry, and syenogranite units (178.6 ± 2.2–175.6 ± 3.0 Ma) are indistinguishable from the mean molybdenite Re-Os model and hydrothermal biotite $^{40}Ar/^{39}Ar$ plateau ages within uncertainty (Fig. 15), indicating that these three units most likely are synmineralization intrusions. This interpretation is supported by the fact that the porphyritic monzogranite, granite porphyry, and syenogranite units all host EB-, A-, and B-type veins, confirming a genetic link for these units with Mo mineralization (e.g., Seedorff and Einaudi, 2004; Seedorff et al., 2005, 2008).

Pulsed veining accompanies multiple cycles of synmineralization intrusion emplacement

In porphyry systems, veins and breccias form throughout the lifetime of the magmatic-hydrothermal system and represent the locus of fluid flux (Seedorff et al., 2005; Sillitoe, 2010). Hence, vein and breccia mineralogy, texture, location, and abundance can provide valuable constraints on the space-time evolution of fluid flow and related magmatic activity (e.g., Gustafson and Quiroga, 1995; Muntean and Einaudi, 2001; Seedorff and Einaudi, 2004; Chang et al., 2017; Braxton et al., 2018; Cao et al., 2019).

Vein truncation relationships between the multiple vein types identified in this study indicate that biotite veins with potassic alteration (i.e., EB-type veins) and quartz ± biotite veins with or without potassic envelopes (i.e., A-type veins) are the two earliest vein types at Luming (Fig. 7). They are only observed in relatively low abundance in the synmineralization porphyritic monzogranite, granite porphyry, and syenogranite units with a common feature that EB-type veins predate A-type veins (Figs. 8, 9). As no truncation relationships between these high-temperature veins and successive productive intrusive units were observed in this study (e.g., EB- and/or A-type veins hosted in the porphyritic monzogranite unit were truncated by the late granite porphyry or syenogranite unit; Sillitoe, 2010), there is a possibility that these high-temperature veins were formed from a continuous flux of ore-bearing hydrothermal fluids as implicitly or explicitly stated in many previous studies (e.g., Shi et al., 2007; Ma and Chen, 2012; Tan et al., 2012; Hu et al., 2014; Liu et al., 2014; Cheng et al., 2015; Xi et al., 2018). However, we discount this possibility based on (1) repetitions of B- and D-type veins, which are infrequently repeated in a single magmatic-hydrothermal pulse event in porphyry systems (Sillitoe, 2010), yet occur in both pre- and synmineralization intrusive units of the Luming deposit (Fig. 7); (2) reverse crosscutting relationships (e.g., early A2 veins are crosscut by late A2 veins, Fig. 8d; B-type veins are crosscut by A1 veins, Fig. 9d), which provide robust evidence for multipulsed magmatic-hydrothermal events (Seedorff and Einaudi, 2004; Seedorff et al., 2005), were observed in the synmineralization porphyritic monzogranite and granite porphyry units; (3) the magmatic-hydrothermal breccias contain clasts of mineralized porphyritic monzogranite and quartz-molybdenite fragments, which are encased within D-type quartz-molybdenite ± pyrite veins (Fig. 11c, e), suggesting there may have been more than one pulse of venting; and (4) the synmineralization intrusive units cut B-type veins hosted in the premineralization intrusions and are in turn cut by other A- and D-type veins (e.g., Fig. 7c), indicating at least two veining events.

Further evidence for multiple pulses of veining at Luming lies in the irregular alteration pattern and development of a magmatic-hydrothermal breccia body in the synmineralization porphyritic monzogranite unit. As shown in Figures 3 and 11, there is a pervasive alteration zone (up to 400 m thick) in the porphyritic monzogranite unit, which is characterized by the complete replacement of porphyritic monzogranite by secondary K-feldspar with relics of quartz and K-feldspar phenocrysts and overprinted by feldspar-destructive (phyllic and propylitic) alteration; in the magmatic-hydrothermal breccia body, clasts of porphyritic monzogranite are overprinted by high-intensity alteration comprising potassic and sericitic overgrowths. These two characteristics are different from the porphyry systems formed by a single magmatic-hydrothermal pulse event as described by Lowell and Guibert (1970) and Sillitoe (2010), in which intensive potassic alteration commonly affects the upper part of the synmineralization intrusion and its contiguous host rocks, and magmatic-hydrothermal breccia bodies are typically hosted within premineralization intrusions. Taken together, the evidence presented above suggests that the Luming system was formed by pulsed veining associated with multiple cycles of synmineralization intrusion emplacement.

Pulsed veining enhanced molybdenum endowment of the Luming deposit

In the Luming deposit, the premineralization biotite monzogranite and monzogranite units host the bulk of the molybdenum orebodies (more than 65%; Yichun Luming Ming

Co., LTD, unpub. data, 2010; Figs. 3–5). Molybdenite mineralization in these two units, which dominantly occurs in the form of D1- and D2-type veins (Figs. 7, 10), appears as shells surrounding the synmineralization porphyritic monzogranite unit, which hosts high-temperature EB-, A-, and B-type veins (Figs. 3–5, 7, 8). This intrusion-vein-mineralization relationship indicates that molybdenite mineralization in the biotite monzogranite and monzogranite units likely resulted from the fluid flux sourced from the porphyritic monzogranite unit, as observed in many porphyry Mo systems (e.g., Leng et al., 2015; Ouyang et al., 2020). However, vein truncation relationships in the premineralization units precluded this theory. As shown in Figure 10, the premineralization biotite monzogranite unit contains D1- and D2-type veins exhibiting reverse crosscutting relationships (e.g., early D1 or D2 veins are crosscut by late D1 or D2 veins). The implication of these reverse, infrequently repeated veins is the existence of superimposed molybdenite mineralization at Luming, probably relating to the successive synmineralization porphyritic monzogranite, granite porphyry and/or syenogranite units. This interpretation is supported by the pattern of Mo mineralization distribution in the Luming deposit. As shown in Figures 4 and 5, molybdenite-bearing assemblages (i.e., quartz-molybdenite ± pyrite and molybdenite ± pyrite) at Luming exhibit multiple high-grade zones (>0.06 wt % Mo), which in turn, to some extent, coincide spatially with the emplacement of individual synmineralization intrusive units. Other evidence for supporting molybdenite mineralization superimposition lies in the atypical mineralization features of the synmineralization intrusions in the Luming deposit. For example, ore-grade assay and drilling core logging data show that nearly one-third of the mineralized zone in the Luming deposit is localized within the productive porphyritic monzogranite unit in the form of B- and D-type veins (Yichun Luming Ming Co., LTD, unpub. data, 2010; Figs. 3–5, 8; Table 1), which is rare in porphyry systems associated with a single magmatic-hydrothermal pulse event (e.g., Sillitoe, 2010; Reed et al., 2013; Leng et al., 2015; Ouyang et al., 2020). In the synmineralization porphyritic monzogranite and granite porphyry units, there is repetition of molybdenite-bearing B- and D-type veins (Figs. 7–9), indicating that the emplacement of the granite porphyry and syenogranite units also induced molybdenite-bearing veining, superimposed on earlier intrusions and mineralization. The sum of the observations mentioned above suggests that the fluid fluxes associated with the emplacement of the synmineralization porphyritic monzogranite, granite porphyry, and syenogranite units may all have contributed successively to produce the observed Mo mineralization at Luming. We thus conclude that repeated cycles of magmatic and hydrothermal events associated with the synmineralization porphyritic monzogranite, granite porphyry, and syenogranite units enhanced molybdenum endowment of the Luming deposit. However, the relative proportions contributed by each pulse of magmatic-hydrothermal activity cannot be conclusively determined at this stage.

Pulsed veining and Mo mineralization of large to giant porphyry Mo systems

The above discussion shows that the giant Luming porphyry Mo deposit was formed by the overprinting of successive magmatic-hydrothermal fluids from three synmineralization intrusive units. The question then arises whether the processes (i.e., repeated cycles of magmatic-hydrothermal activity) identified in the Luming deposit hold for other large to giant porphyry Mo deposits worldwide. As there are two major types of porphyry Mo deposits in the world, i.e., Climax type (Ludington and Plumlee, 2009) and arc related (Taylor et al., 2012), to tackle this question, we first need to discuss if there are fundamental differences in the processes controlling ore formation between these two different types of deposits. Notably, Chen et al. (2017a) introduced a third class of porphyry Mo deposits—the Dabie type or collision related—based on the studies of the Late Jurassic to Early Cretaceous porphyry Mo deposits in the Qinling-Dabie orogen, China. However, this classification invites scrutiny as the tectonic setting of the Qinling-Dabie orogen during the Late Jurassic to Early Cretaceous remains controversial (e.g., Mao et al., 2011a, b; Zhang et al., 2014; Chen et al., 2017a; Wang et al., 2018). For this reason, the Dabie-type porphyry Mo deposits will not be taken into account in the following discussion.

It is known that the majority of Climax-type Mo deposits are associated with fluorine-rich, highly evolved rhyolitic intrusions in extensional postsubduction settings (Carten et al., 1993; Ludington and Plumlee 2009); arc-related Mo deposits are commonly related to fluorine-poor, differentiated calc-alkaline granitoids in compressional arc-continent subduction and collision or continent-continent collision settings (Carten et al., 1993; Taylor et al., 2012). The association of the two types of porphyry Mo deposits with distinct tectonic settings and magma compositions could suggest some sort of petrogenetic control. Recently it has become evident that magmas associated both with Climax-type and arc-related porphyry Mo deposits are Mo poor (2–25 ppm; Lerchbaumer and Audétat, 2013; Audétat and Li, 2017; Zhang and Audétat, 2018; Ouyang et al., 2020; this study), oxidized (above the quartz-fayalite-magnetite buffer; Zhang and Audétat, 2017; Ouyang et al., 2020), and water saturated, with magma emplacement depth between 1 and 6 km (Audétat and Li, 2017, and references therein; Ouyang et al., 2020), regardless of magma source (e.g., crust-derived, mantle-derived, or mixed sources) and composition (e.g., volatile content and extent of fractionation; Ouyang et al., 2020). These data most likely support the concept of fundamentally similar processes of ore formation between the arc-related and Climax-type porphyry Mo deposits (e.g., Carten et al., 1993; Lerchbaumer and Audétat, 2013; Audétat and Li, 2017; Zhang and Audétat, 2018; Ouyang et al., 2020). In the meantime, the data presented above highlight the fundamental role of magma oxygen fugacity, water content, and emplacement depth (also indicated by the porphyritic texture of the causative intrusions) as prerequisite controls for the formation of porphyry Mo deposits.

Previous studies indicated that in order to form a large to giant porphyry Mo deposit, large volumes of oxidized and water-saturated magmas are needed, as the volume of magma determines the maximum amount of deliverable molybdenum (e.g., Lerchbaumer and Audétat, 2013; Zhang and Audétat, 2017; Ouyang et al., 2020). On the other hand, melt and fluid inclusion studies on barren and subeconomic intrusions with dimensions of over 230 km^3, large enough to form giant Mo deposits, show that (1) the barren and subeconomic intrusions are also oxidized and water saturated, with magma emplace-

ment depths similar to those of fertile intrusions (Lerchbaumer and Audétat, 2013; Zhang and Audétat, 2018; Ouyang et al., 2020), and (2) there are no significant variations in Mo contents of the high-temperature fluids exsolved from the barren and fertile intrusions (Lerchbaumer and Audétat, 2013; Audétat, 2015, 2019; Audétat and Li, 2017; Zhang and Audétat, 2018). The two results above suggest that, in addition to a large volume of magma, other additional processes may be required to form a large to giant porphyry Mo deposit. The processes include (1) focused emplacement of magmas (e.g., Audétat and Li, 2017) and (2) long-lived magmatic-hydrothermal activities (e.g., Seedorff et al., 2005; Chiaradia and Caricchi, 2017; Chiaradia, 2020), which are, in turn, most likely fulfilled through pulsed veining and mineralization associated with small intrusions. This inference is consistent with field observations in a number of large to giant porphyry Mo deposits, irrespective of their genetic affiliation (arc-related vs. Climax type). For instance, studies on the Climax-type Henderson deposit (1.07 Mt Mo) showed that this deposit was formed by the superposition of coupled alteration and mineralization events that were associated with 12 small rhyolitic stocks (Carten et al., 1988; Seedorff and Einaudi, 2004). Similarly, the ore shells in the Climax deposit (2.20 Mt Mo) were produced by multiple discrete small stocks, which were separated spatially (Bookstrom et al., 1988). Molybdenum mineralization at the Climax-type Questa deposit (0.44 Mt Mo) is suggested to have occurred through pulsed emplacement of at least six small felsic intrusions that lasted ca. 500 k.y. (Gaynor et al., 2019a). The arc-related Endako deposit (0.41 Mt Mo) is considered to have formed by episodic emplacement of six granodioritic intrusions over 9 m.y. (Selby and Creaser, 2001; Villeneuve et al., 2001). These observations suggest that many large to giant porphyry Mo deposits, irrespective of their genetic affiliation, display a pulsed veining and mineralization characteristic that is similar to the formation of the giant arc-related Luming Mo deposit and differs from the standard model of porphyry Mo deposits formed by a single magmatic-hydrothermal pulse (Sillitoe, 2010; Taylor et al., 2012). We thus propose that repeated cycles of magmatic-hydrothermal activity play an important role in the generation of large to giant porphyry Mo deposits of both the arc-related and Climax type.

In fact, multiple pulses of veining and mineralization are also associated with large to giant (≥2.0 Mt Cu; Yang and Cooke, 2019) porphyry Cu deposits, including the Yerington mine, USA (Dilles et al., 2000); Chuquicamata, Chile (Ballard et al., 2001); El Teniente, Chile (Vry et al., 2010); Yulong, China (Chang et al., 2017); Boyongan and Bayugo, Philippines (Braxton et al., 2018); and Pulang, China (Cao et al., 2019). The role of multiple magmatic-hydrothermal pulses for the development of large to giant porphyry Cu systems is beyond the scope of this study; however, notably, the giant El Teniente, Chuquicamata, and Yulong porphyry Cu deposits have all been ascribed to the superposition of multiple magmatic-hydrothermal pulses (Ballard et al., 2001; Vry et al., 2010; Chang et al., 2017).

The nature of repeated cycles of magmatic-hydrothermal events in large to giant porphyry Mo systems

Our melt inclusion data show that the melts from the syn-mineralization intrusions at Luming contain less than 4 ppm Mo (Fig. 14). These values are comparable with data obtained from subduction-related porphyry Mo deposits (Ouyang et al., 2020) and barren intrusions (Zhang and Audétat, 2018) but are at the lower end of the range displayed by Climax-type deposits and subeconomic intrusions (Audétat and Li, 2017). However, all values reflect the Mo-poor nature of the ore-forming magmas in porphyry Mo systems (mostly <25 ppm; Fig. 14). Recently acquired fluid inclusion data show that the Mo concentrations of primary exsolved fluids in economic porphyry systems and barren felsic intrusions are similar, with values of ~100 ppm (Lerchbaumer and Audétat, 2013; Audétat, 2019). These results indicate that substantial volumes of magma and fluids are needed to form large to giant porphyry Mo deposits. For example, assuming the ore-forming magmas have a density of 2.4 g/cm^3 (Fountain and Christensen, 1989) and Mo concentration of 4 ppm, and assuming 100% extraction and precipitation efficiency of Mo from the magmas, to account for the 0.75 Mt of Mo present in the Luming deposit at least 78 km^3 of magma is necessary. Meanwhile, at least 11 km^3 of intermediate-density fluids are needed, assuming the fluid contains 100 ppm Mo (Audétat, 2019) and assuming 100% precipitation efficiency of Mo from the fluids. However, as discussed in the previous section, other critical factors, which perhaps can enhance the mineralization potential and rise the metal tonnages of porphyry Mo deposits, include the size and/or shape of the ensuing causative intrusions (e.g., Audétat and Li, 2017; Schöpa et al., 2017; Gaynor et al., 2019a; Ouyang et al., 2020), as they act as the conduits through which deep seated magmas with fluid and molybdenum cargoes are transferred to the site of mineralization (Lowenstern, 1994; Dilles et al., 2000; Seedorff et al., 2005). If fluids from the underlying magma reservoir vent within a broad intrusion rather than via a cupola or other focusing structure, then the fluid flow may be insufficiently focused to lead to economic ore formation, as is considered the case for the Huangshan felsic pluton (Zhang and Audétat, 2018) and the Yerington batholith (Schöpa et al., 2017), or may lead to diffuse, low-grade mineralization, as is the case for the subeconomic Treasure Mountain granite (Lerchbaumer and Audétat, 2013). Mineralization is considered to form favorably when fluids released from the magma chamber are channeled toward the upper crust along small igneous intrusive bodies (Audétat and Li, 2017; Gaynor et al., 2019a; Ouyang et al., 2020). This argument is consistent with field observations whereby causative intrusions in porphyry systems are commonly small with diameters of less than 500 m (Carten et al., 1988; Dilles et al., 2000; Cooke et al., 2005; Seedorff et al., 2005, 2008; Sillitoe, 2010; Gaynor et al., 2019a; this study). Results of numerical calculations show that the timescale of hydrothermal activity that can be sustained by a single magmatic-hydrothermal pulse event is limited to (several) tens of thousands of years (Cathles et al., 1997; Mercer et al., 2015), consistent with recent high-precision molybdenite Re-Os dating results from numerous porphyry systems (e.g., Chiaradia et al., 2013, and references therein; Rosera et al., 2013; Li et al., 2017). This could imply that the volume of fluids transferred from an underlying magma chamber to the site of mineralization via a single pulse of small intrusion emplacement is finite. In the meantime, it suggests that to raise the tonnage and/or grade of mineralization, cyclic emplacement of small intrusions along with multiple pulses of fluid

exsolution are required. This conclusion is consistent with the observed reversals in magmatic-hydrothermal evolutionary trend (e.g., Seedorff and Einaudi, 2004; this study) and the relatively long total duration (e.g., 500 k.y. at Questa; Gaynor et al., 2019a) of hydrothermal activity within many large to giant porphyry Mo deposits of both the arc-related and Climax type (e.g., Selby and Creaser, 2001; Gaynor et al., 2019a).

Conclusions

The Luming porphyry Mo deposit is hosted by a composite complex composed of five major, successive granitic intrusive units: the biotite monzogranite, monzogranite, porphyritic monzogranite, granite porphyry, and syenogranite. The latter three units are closely associated with Mo mineralization, have progressively smaller volumes, and are more deeply and centrally emplaced within the composite complex. Vein-intrusion truncation relationships show that each synmineralization intrusion emplacement event was followed by a similar and successive sequence of veining that complies with the general order of early EB-type veins, through A- and B-type veins, to late D-type veins. Results of LA-ICP-MS dating of zircon indicate that the intrusion ages of the premineralization units are between 187.5 ± 2.8 and 186.5 ± 3.6 Ma (2σ), and those of the synmineralization units range from 178.6 ± 2.2 to 175.6 ± 3.0 Ma (2σ). Hydrothermal biotite from EB-type veins hosted in the syenogranite unit yielded a $^{40}Ar/^{39}Ar$ plateau age of 174.7 ± 1.1 Ma (2σ). Melt inclusion data show that the Mo concentrations of the synmineralization intrusions are <4 ppm. Crosscutting relationships indicate that mineralizing events in the Luming deposit were episodic and can be synthesized into a model in which sequential emplacement of three Mo-poor synmineralization intrusions is accompanied by a separate mineralization and alteration event. We conclude that pulsed release of ore-forming magmas and fluids, which are channeled along focusing structures like small porphyry fingers within a focused area, from a magma chamber at depth may be an important factor for the formation of large to giant porphyry Mo deposits of both the arc-related and Climax type.

Acknowledgments

This research was supported by National Key Research and Development Plan (grant 2017YFC0601403), Scientific Research Fund of the China Central Non-Commercial Institute (KK2013, K1707, and KK1414), National Science Foundation of China (41820104010, 41772084, and 41902094), and International Postdoctoral Exchange Fellowship Program of China Postdoctoral Council (20170032). We thank Andreas Audétat for helping with melt inclusion LA-ICP-MS analyses and Chao Li (National Research Center for Geoanalysis, Chinese Academy of Geological Sciences) and Liang Li (Nanjing FocuMS Technology Co. Ltd.) for assisting with the calculation and interpretation of molybdenite Re-Os and zircon U-Pb data. Constructive comments from Massimo Chiaradia, Sean Gaynor, and the editor, Larry Meinert, are greatly appreciated.

REFERENCES

Audétat, A., 2015, Compositional evolution and formation conditions of magmas and fluids related to porphyry Mo mineralization at Climax, Colorado: Journal of Petrology, v. 56, p. 1519–1546.

——2019, The metal content of magmatic-hydrothermal fluids and its relationship to mineralization potential: Economic Geology, v. 114, p. 1033–1056.

Audétat, A., and Li, W.T., 2017, The genesis of Climax-type porphyry Mo deposits: Insights from fluid inclusions and melt inclusions: Ore Geology Reviews, v. 88, p. 436–460.

Audétat, A., Pettke, T., Heinrich, C.A., and Bodnar, R.J., 2008, Special Paper: The composition of magmatic-hydrothermal fluids in barren and mineralized intrusions: Economic Geology, v. 103, p. 877–908.

Ballard, J.R., Palin, J.M., Williams, I.S., Campbell, I.H., and Faunes, A., 2001, Two ages of porphyry intrusion resolved for the super-giant Chuquicamata copper deposit of northern Chile by ELA-ICP-MS and SHRIMP: Geology, v. 29, p. 383–386.

Black, L.P., and Gulson, B.L., 1978, The age of the Mud Tank carbonatite, Strangways Range, Northern Territory BMR: Journal of Australian Geology and Geophysics, v. 3, p. 227–232.

Bookstrom, A.A., 1989, The Climax-Alma granite batholith of Oligocene age and the porphyry molybdenum deposits of Climax, Colorado, U.S.A.: Engineering Geology, v. 27, p. 543–568.

Bookstrom, A.A., Carten, R.B., Shannon, J.R., and Smith, R.P., 1988, Origins of bimodal leucogranite-lamprophyre suites, Climax and Red Mountain porphyry molybdenum systems, Colorado: Petrologic and strontium isotopic evidence: Colorado School of Mines Quarterly, v. 83, p. 1–22.

Braxton, D.P., Cooke, D.R., Ignacio, A.M., and Waters, P.J., 2018, Geology of the Boyongan and Bayugo porphyry Cu-Au deposits: An emerging porphyry district in northeast Mindanao, Philippines: Economic Geology, v. 113, p. 83–131.

Cao, K., Yang, Z.M., Mavrogenes, J., White, N.C., Xu, J.F., Li, Y., and Li, W.K., 2019, Geology and genesis of the giant Pulang porphyry Cu-Au district, Yunnan, Southwest China: Economic Geology, v. 114, p. 275–301.

Carten, R.B., Geraghty, E.P., Walker, B.M., and Shannon, J.R., 1988, Cyclic development of igneous features and their relationship to high-temperature hydrothermal features in the Henderson porphyry molybdenum deposit, Colorado: Economic Geology, v. 83, p. 266–296.

Carten, R.B., White, W.H., and Stein, H.J., 1993, High-grade granite-related molybdenum systems: Classification and origin: Geological Association of Canada Special Paper, v. 40, p. 521–554.

Cathles, L.M., Erendi, A.H.J., and Barrie, T., 1997, How long can a hydrothermal system be sustained by a single intrusive event?: Economic Geology, v. 92, p. 766–771.

Chang, J., Li, J.W., Selby, D., Liu, J.C., and Deng, X.D., 2017, Geological and chronological constraints on the long-lived Eocene Yulong porphyry Cu-Mo deposit, Eastern Tibet: Implications for the lifespan of giant porphyry Cu deposits: Economic Geology, v. 112, p. 1719–1746.

Chelle-Michou, C., Chiaradia, M., Selby, D., Ovtcharova, M., and Spikings, R.A., 2015, High-resolution geochronology of the Coroccohuayco porphyry-skarn deposit, Peru: A rapid product of the Incaic orogeny: Economic Geology, v. 110, p. 423–443.

Chelle-Michou, C., Rottier, B., Caricchi, L., and Simpson, G., 2017, Tempo of magma degassing and the genesis of porphyry copper deposits: Scientific Reports, doi: 10.1038/srep40566.

Chen, W., Wan, Y.S., Li, H.Q., and Zhang, Z.Q., 2012, Isotope geochronology: Technique and application: Acta Geologica Sinica, v. 85, p. 1917–1947.

Chen, Y.J., Wang, P., Li, N., Yang, Y.F., and Pirajno, F., 2017a, The collision-type porphyry Mo deposits in Dabie Shan, China: Ore Geology Reviews, v. 81, p. 405–430.

Chen, Y.J., Zhang, C., Wang, P., Pirajno, F., and Li, N., 2017b, The Mo deposits of northeast China: A powerful indicator of tectonic settings and associated evolutionary trends: Ore Geology Reviews, v. 81, p. 602–640.

Cheng, G.H., Wang, R.L., Zeng, Q.D., Guo, Y.P., Duang, X.X., Wei, J.J., Zhang, J.S., and Gao, X.H., 2015, Zircon U-Pb ages, Hf isotopes of the granitoids and Re-Os ages of the molybdenites in Luming molybdenum ore area, Heilongjiang province, and its geological significance: Acta Petrologica Sinica, v. 31, p. 2450–2464 (in Chinese with English abs.).

Chiaradia, M., 2020, Gold endowments of porphyry deposits controlled by precipitation efficiency: Nature Communications, doi: 10.1038/s41467-019-14113-1.

Chiaradia, M., and Caricchi, L., 2017, Stochastic modelling of deep magmatic controls on porphyry copper deposit endowment: Scientific Reports, doi: 10.1038/srep44523.

Chiaradia, M., Schaltegger, U., Spikings, R., Wotzlaw, J.F., and Ovtcharova, M., 2013, How accurately can we date the duration of magmatic-hydrothermal

events in porphyry systems?—an invited paper: Economic Geology, v. 108, p. 565–584.
Cooke, D.R., Hollings, P., and Walshe, J.L., 2005, Giant porphyry deposits: Characteristics, distribution, and tectonic controls: Economic Geology, v. 100, p. 801–818.
Dilles, J.H., Einaudi, M.T., Proffett, J., and Barton, M.D., 2000, Overview of the Yerington porphyry copper district: Magmatic to nonmagmatic sources of hydrothermal fluids, their flow paths, alteration affects on rocks, and Cu-Mo-Fe-Au ores: Society of Economic Geologists Guidebook Series, v. 32, p. 55–66.
Fountain, D.M., and Christensen, N.I., 1989, Composition of the continental crust and upper mantle: A review: Geophysical Framework of the Continental United States, v. 172, p. 711–742.
Gaynor, S.P., Rosera, J.M., and Coleman, D.S., 2019a, Intrusive history of the Oligocene porphyry molybdenum deposit, New Mexico: Geosphere, v. 15, p. 548–575.
Gaynor, S.P., Coleman, D.S., Rosera, J.M., and Tappa, M.J., 2019b, Geochronology of a Questa bouguer gravity low: Journal of Geophysical Research: Solid Earth, v. 124, p. 2457–2468.
Gustafson, L.B., and Hunt, J.P., 1975, The porphyry copper deposit at El Salvador, Chile: Economic Geology, v. 70, p. 857–912.
Gustafson, L.B., and Quiroga, J., 1995, Patterns of mineralization and alteration below the porphyry copper orebody at El Salvador, Chile: Economic Geology, v. 90, p. 2–16.
Hu, X.L., Ding, Z.J., He, M.C., Yao, S.Z., Zhu, B.P., Shen, J., and Chen, B., 2014, A porphyry-skarn metallogenic system in the Lesser Xing'an Range, NE China: Implications from U-Pb and Re-Os geochronology and Sr-Nd-Hf isotopes of the Luming Mo and Xulaojiugou Pb-Zn deposits: Journal of Asian Earth Sciences, v. 90, p. 88–100.
Hu, Z.C., Liu, Y.S., Chen, L., Zhou, L., Li, M., Zong, K.Q., Zhu, L.Y., and Gao, S., 2011, Contrasting matrix induced elemental fractionation in NIST SRM and rock glasses during laser ablation ICP-MS analysis at high spatial resolution: Journal of Analytical Atomic Spectrometry, v. 26, p. 425–430.
Lee, J.Y., Marti, K., Severinghaus, J.P., Kawamura, K., Yoo, H.S., Lee, J.B., and Kim, J.S., 2006, A redetermination of the isotopic abundances of atmospheric Ar: Geochimica et Cosmochimica Acta, v. 70, p. 4507–4512.
Leng, C.B., Zhang, X.C., Huang, Z.L., Huang, Q.Y., Wang, S.X., Ma, D.Y., Luo, T.Y., Li, C., and Li, W.B., 2015, Geology, Re-Os ages, sulfur and lead isotopes of the Diyanqinamu porphyry Mo deposit, Inner Mongolia, NE China: Economic Geology, v. 110, p. 557–574.
Lerchbaumer, L., and Audétat, A., 2013, The metal content of silicate melts and aqueous fluids in subeconomically Mo mineralized granites: Implications for porphyry Mo genesis: Economic Geology, v. 108, p. 987–1013.
Li, S.C., Han, Z.Z., Niu, Y.H., Zhang, Y.L., Wang, X., Chen, S.X., and Zheng, T., 2015, Determination of ages of metallogenic monzonitic intrusion and geological implication in the Xilin Pb-Zn-Fe ore deposit, Yichun, Heilongjiang province granite: Mineral Exploration, v. 6, p. 356–363 (in Chinese with English abs.).
Li, Y., Selby, D., Condon, D., and Tapster, S., 2017, Cyclic magmatic-hydrothermal evolution in porphyry systems: High-precision U-Pb and Re-Os geochronology constraints on the Tibetan Qulong porphyry Cu-Mo deposit: Economic Geology, v. 112, p. 1419–1440.
Liu, C., Deng, J.F., Luo, Z.H., Tian, S.P., Zhang, Y., Zhong, C.T., and Zhao, H.D., 2014, Post-batholith metallogenesis: Evidence from Luming super large molybdenite deposit in Lesser Xing'an Range: Acta Petrologica Sinica, v. 30, p. 3400–3418 (in Chinese with English abs.).
Liu, Y.S., Hu, Z.C., Zong, K.Q., Gao, C.G., Gao, S., Xu, J., and Chen, H.H., 2010, Reappraisement and refinement of zircon U-Pb isotope and trace element analyses by LA-ICP-MS: Chinese Science Bulletin, v. 55, p. 1535–1546.
Lowell, J.D., and Guilbert, J.M., 1970, Lateral and vertical alteration-mineralization zoning in porphyry ore deposits: Economic Geology, v. 65, p. 373–408.
Lowenstern, J.B., 1994, Dissolved volatile concentrations in an ore-forming magma: Geology, v. 22, p. 893–896.
Ludington, S., and Plumlee, G.S., 2009, Climax-type porphyry molybdenum deposits: U.S. Geological Survey, Open-File Report 2009-1215, p. 16.
Ludwig, K.R., 2003, Isoplot 3.00: A geochronological toolkit for Microsoft Excel: Berkeley Geochronology Center, Special Publication 5, 70 p.
Ma, S.Q., and Chen, J., 2012, Geochronology and geochemistry of granite of the Luming molybdenum deposit in Heilongjiang and their geological significance: Geology in China, v. 39, p. 1162–1171 (in Chinese with English abs.).
Mao, J.W., Pirajno, F., Xiang, J.F., Gao, J.J., Ye, H.S., Li, Y.F., and Guo, B.J., 2011a, Mesozoic molybdenum deposits in the east Qinling-Dabie orogenic belt: Characteristics and tectonic settings: Ore Geology Reviews, v. 43, p. 264–293.
Mao, J.W., Pirajno, F., and Cook, N., 2011b, Mesozoic metallogeny in East China and corresponding geodynamic settings: An introduction to the special issue: Ore Geology Reviews, v. 43, p. 1–7.
Mercer, C.N., Reed, M.H., and Mercer, C.M., 2015, Time scales of porphyry Cu deposit formation: Insights from titanium diffusion in quartz: Economic Geology, v. 110, p. 587–602.
Miller, J.S., Matzel, J.E.P., Miller, C.F., Burgess, S.D., and Miller, R.B., 2007, Zircon growth and recycling during the assembly of large, composite arc plutons: Journal of Volcanology and Geothermal Research, v. 167, p. 282–299.
Muntean, J.L., and Einaudi, M.T., 2001, Porphyry-epithermal transition: Maricunga belt, northern Chile: Economic Geology, v. 96, p. 743–772.
Ouyang, H.G., Mao, J.W., Santosh, M., Zhou, J., Zhou, Z.H., Wu, Y., and Hou, L., 2013, Geodynamic setting of Mesozoic magmatism in NE China and surrounding regions: Perspectives from spatio-temporal distribution patterns of ore deposits: Journal of Asian Earth Sciences, v. 78, p. 222–236.
Ouyang, H.G., Che, X.G., and Zhou, Z.H., 2016, ^{40}Ar-^{39}Ar dating of Ergu Fe-polymetallic skarn deposit in Yichun igneous belt and its geological implications: Mineral Deposits, v. 5, p. 1035–1046 (in Chinese with English abs.).
Ouyang, H.G., Mao, J.W., and Hu, R.Z., 2020, Geochemistry and crystallization conditions of magmas related to porphyry Mo mineralization in northeastern China: Economic Geology, v. 115, p. 79–100.
Pettke T., Oberli F., and Heinrich C.A., 2010, The magma and metal source of giant porphyry-type ore deposits, based on lead isotope microanalysis of individual fluid inclusions: Earth and Planetary Science Letters, v. 296, p. 267–277.
Redmond, P.B., and Einaudi, M.T., 2010, The Bingham Canyon porphyry Cu-Mo-Au deposit. I. Sequence of intrusions, vein formation, and sulfide deposition: Economic Geology, v. 105, p. 43–68.
Reed, M., Rusk, B., and Palandri, J., 2013, The Butte magmatic-hydrothermal system: One fluid yields all alteration and veins: Economic Geology, v. 108, p. 1379–1396.
Richards, J.P., 2013, Giant ore deposits formed by optimal alignments and combinations of geological processes: Nature Geoscience, doi: 10.1038/NGEO1920.
Rosera, J.M., Coleman, D.S., and Stein, H.J., 2013, Re-evaluating genetic models for porphyry Mo mineralization at Questa, New Mexico; implications for ore deposition following silicic ignimbrite eruption: Geochemistry, Geophysics, Geosystems, v. 14, p. 787–805.
Schaltegger, U., Schmitt, A.K., and Horstwood, M.S.A., 2015, U-Th-Pb zircon geochronology by ID-TIMS, SIMS, and laser ablation ICP-MS: Recipes, interpretations, and opportunities: Chemical Geology, v. 402, p. 89–110.
Schöpa, A., Annen, C., Dilles, J.H., Sparks, R.S.J., Blundy, J.D., 2017, Magma emplacement rates and porphyry copper deposits: Thermal modeling of the Yerington batholith, Nevada: Economic Geology, v. 112, p. 1653–1672.
Seedorff, E., and Einaudi, M.T., 2004, Henderson porphyry molybdenum system, Colorado: I. Sequence and abundance of hydrothermal mineral assemblages, flow paths of evolving fluids, and evolutionary style: Economic Geology, v. 99, p. 3–37.
Seedorff, E., Dilles, J.H., Proffett, J.M., Jr., Einaudi, M.R., Zurcher, L., Stavast, W.J.A., Johnson, D.A., and Barton, M.D., 2005, Porphyry copper deposits: Characteristics and origin of hypogene features: Economic Geology 100th Anniversary Volume, p. 251–298.
Seedorff, E., Barton, M.D., Stavast, W.J.A., and Mather, D.J., 2008, Root zones of porphyry systems: Extending the porphyry model to depth: Economic Geology, v. 103, p. 939–956.
Selby, D., and Creaser, R.A., 2001, Re-Os geochronology and systematics in molybdenite from the Endako porphyry molybdenum deposit, British Columbia, Canada: Economic Geology, v. 96, p. 197–204.
Shao, J., Yang, H.Z., Jia, B., and Peng, M.S., 2012, Geological characteristics and ore-forming age of Luming Mo deposit in Heilongjiang province: Mineral Deposits, v. 31, p. 1301–1310 (in Chinese with English abs.).
Shi, Y.M., Cui, B., and Jia, W.L., 2007, Geology of the Luming Mo deposit, Tieli, Heilongjiang province: Geology and Prospecting, v. 43, p. 19–22 (in Chinese with English abs.).
Shu, Q.H., Chang, Z.S., Lai, Y., Zhou, Y.T., Sun, Y., and Yan, C., 2016, Regional metallogeny of Mo-bearing deposits in northeastern China, with

new Re-Os dates of porphyry Mo deposits in the northern Xilamulun district: Economic Geology, v. 111, p. 1783–1798.
Sillitoe, R.H., 2010, Porphyry copper systems: Economic Geology, v. 105, p. 3–41.
Steiger, R.H., and Jäger, E., 1977, Subcommission on geochronology: Convention on the use of decay constants in geo- and cosmochronology: Earth and Planetary Science Letters, v. 36, p. 359–362.
Sun, Q.L., Sun, J.G., Zhao, K.Q., Tang, C., Zhang, Y., Han, S.J., and Yang, F., 2014, Re-Os isotopic dating and geological significance of Luming porphyry molybdenum deposit in Heilongjiang: Global Geology, v. 33, p. 418–426 (in Chinese with English abs.).
Tan, H.Y., Shu, G.L., Lu, J.C., Han, R.P., Zhang, S., and Kou, L.L., 2012, LA-ICP-MS zircon U-Pb and molybdenite Re-Os dating for the Luming large-scale molybdenum deposit in Xiao Hinggan Mountains and its geological implication: Journal of Jilin University (Earth Science Edition), v. 42, p. 1757–1770 (in Chinese with English abs.).
Taylor, R.D., Hammarstrom, J.M., Piatak, N.M., and Seal II, R.R., 2012, Arc-related porphyry molybdenum deposit model: U.S. Geological Survey, Scientific Investigations Report 2010-5070-D, p. 51.
Villeneuve, M., Whalen, J.B., Anderson, R.G., and Struik, L.C., 2001, The Endako batholith: Episodic plutonism culminating in formation of the Endako porphyry molybdenite deposit, north-central British Columbia: Economic Geology, v. 96, p. 171–196.
Vry, V.H., Wilkinson, J.J., Seguel, J., and Millan, J., 2010, Multistage intrusion, brecciation, and veining at El Teniente, Chile: Evolution of a nested porphyry system: Economic Geology, v. 105, p. 119–153.
Wang, S.S., 1983, Age determinations of ^{40}Ar-^{40}K, ^{40}Ar-^{39}Ar and radiogenic ^{40}Ar released characteristics on K-Ar geostandards of China: Scientia Geologica Sinica, v. 4, p. 315–323 (in Chinese with English abs.).
Wang, Y., Zhou, L.Y., Liu, S.F., Li, J.Y., and Yang, T.N., 2018, Post-cratonization deformation processes and tectonic evolution of the North China craton: Earth-Science Reviews, v. 177, p. 320–365.
Wiedenbeck, M., Alle, P., Corfu, F., Griffin, W.L., Meier, M., Oberli, F., Quadt, A.V., Roddick, J.C., and Spiegel, W., 1995, Three natural zircon standards for U-Th-Pb, Lu-Hf, trace element and REE analyses: Geostandards Newsletter, v. 19, p. 1–23.
Wu, F.Y., Yang, J.H., Lo, C.H., Wilde, S.A., Sun, D.Y., and Jahn, B.M., 2007, The Heilongjiang Group: A Jurassic accretionary complex in the Jiamusi Massif at the western Pacific margin of northeastern China: Island Arc, v. 16, p. 156–172.
Wu, F.Y., Sun, D.Y., Ge, W.C., Zhang, Y.B., Grant, M.L., Wilde, S.A., and Jahn, B.M., 2011, Geochronology of the Phanerozoic granitoids in northeastern China: Journal of Asian Earth Sciences, v. 41, p. 1–30.
Xi, A.H., Ge, Y.H., Liu, J., Xu, B.W., Li, B.L., and Zhu, Y.D., 2018, Discovery of adakite in Tieli Luming-molybdenum miner, Heilongjiang province and its geological implications: Acta Petrologica Sinica, v. 34, p. 719–732 (in Chinese with English abs.).
Xiao, W.J., Windley, B.F., Hao, J., and Zhai, M.G., 2003, Accretion leading to collision and the Permian Solonker suture, Inner Mongolia, China: Termination of the central Asian orogenic belt: Tectonics, doi: 10.1029/2002TC001484.
Xu, W.L., Pei, F.P., Wang, F., Meng, E., Ji, W.Q., Yang, D.B., and Wang, W., 2013, Spatial-temporal relationships of Mesozoic volcanic rocks in NE China: Constraints on tectonic overprinting and transformations between multiple tectonic regimes: Journal of Asian Earth Sciences, v. 74, p. 167–193.
Yang, Z.M., and Cooke, D.R., 2019, Porphyry copper deposits in China: Society of Economic Geologists, Special Publication 22, p. 133–187.
Zhang, D.H., and Audétat, A., 2017, Chemistry, mineralogy and crystallization conditions of porphyry Mo-forming magmas at Urad-Henderson and Silver Creek, Colorado, USA: Journal of Petrology, v. 58, p. 277–296.
——2018, Magmatic-hydrothermal evolution of the barren Huangshan pluton, Anhui province, China: A melt and fluid inclusion study: Economic Geology, v. 113, p. 803–824.
Zhang, S.H., Zhao, Y., Davis, G.A., Ye, H., and Wu, F., 2014, Temporal and spatial variations of Mesozoic magmatism and deformation in the North China craton: Implications for lithospheric thinning and decratonization: Earth-Science Reviews, v. 131, p. 49–87.
Zhao, L., Guo, F., Fan, W.M., and Huang, M.W., 2019, Roles of subducted pelagic and terrigenous sediments in Early Jurassic mafic magmatism in NE China: Constraints on the architecture of Paleo-Pacific subduction zone: Journal of Geophysical Research: Solid Earth, doi: 10.1029/2018JB016487.
Zhu, C.Y., Zhao, G.C., Ji, J.Q., Sun, M., Han, Y.G., Liu, Q., Eizenhöfer, P.R., Zhang, X.R., and Hou, W.Z., 2017, Subduction between the Jiamusi and Songliao blocks: Geological, geochronological and geochemical constraints from the Heilongjiang Complex: Lithos, v. 282, p. 128–144.

Hegen Ouyang is currently an associate professor in the Institute of Mineral Resources, Chinese Academy of Geological Sciences. He received a Ph.D. degree in economic geology from the China University of Geosciences (Beijing) in 2013 and a master's degree from the Institute of Oceanology Chinese Academy of Sciences in 2010. Hegen's research interests include factors affecting porphyry mineralization potential and the temporal and spatial evolution of magmatic-hydrothermal ore systems.